

UNIVERSITY OF CALIFORNIA  
SANTA CRUZ

**SEARCHES FOR ELECTROWEAK PRODUCTION OF  
COMPRESSED SUPERSYMMETRY IN EVENTS WITH SOFT  
LEPTONS PLUS MISSING TRANSVERSE MOMENTUM AND  
HARD JET RECOIL**

A dissertation submitted in partial satisfaction of the  
requirements for the degree of

DOCTOR OF PHILOSOPHY

in

PHYSICS

by

**Sheena Calie Schier**

June 2018

The Dissertation of Sheena Calie Schier  
is approved:

---

Professor Abraham Seiden, Chair

---

Professor Jason Neilsen

---

Professor Michael Hance

---

Dean Tyrus Miller  
Vice Provost and Dean of Graduate Studies

Copyright © by

Sheena Calie Schier

2018

# Table of Contents

<b>List of Figures</b>	<b>vi</b>
<b>List of Tables</b>	<b>xii</b>
<b>Abstract</b>	<b>xiii</b>
<b>Dedication</b>	<b>xiv</b>
<b>Acknowledgments</b>	<b>xv</b>
<b>I First Part</b>	<b>1</b>
<b>1 Introduction</b>	<b>2</b>
<b>2 The Standard Model of Particle Physics and Additional Theories</b>	<b>3</b>
2.1 Forces and Particles . . . . .	3
2.2 Mathematical Formalism of the Standard Model . . . . .	4
2.3 Gauge Symmetries and Spontaneous Symmetry Breaking . . . . .	4
2.4 Higgs Mechanism and Gauge Boson Masses . . . . .	5
2.5 Shortcomings of the Standard Model . . . . .	5
2.5.1 Darkmatter . . . . .	5
2.6 Supersymmetry . . . . .	5
2.7 Phenomenology of Direct Production of Higgsinos and Sleptons in Compressed Scenarios . . . . .	5
<b>3 ATLAS Experiment</b>	<b>6</b>
3.1 Tracking . . . . .	7
3.1.1 Pixel Detector . . . . .	7
3.1.2 Semi-Conductor Tracker . . . . .	7
3.1.3 Transition Radiation Tracker . . . . .	7
3.2 Calorimetry . . . . .	7

3.2.1	Electromagnetic Calorimeter . . . . .	7
3.2.2	Hadronic Calorimeter . . . . .	7
3.3	Muon System . . . . .	7
3.4	DAQ and Trigger . . . . .	8
<b>4</b>	<b>MC and Data samples</b>	<b>9</b>
4.1	Signal Samples . . . . .	9
4.2	Triggers . . . . .	12
4.2.1	MET Triggers . . . . .	12
4.2.2	Combined Triggers . . . . .	12
<b>5</b>	<b>Event Selection and Signal Regions</b>	<b>14</b>
5.1	Object Definitions . . . . .	14
5.2	Discriminating Variables . . . . .	14
5.2.1	Signal Regions . . . . .	17
5.2.2	Slepton Signal Regions . . . . .	17
5.2.3	Higgsino Signal Regions . . . . .	17
<b>6</b>	<b>Fake Factor Method</b>	<b>21</b>
6.1	Introduction . . . . .	22
6.2	Description of Fake Factor Method . . . . .	24
6.3	Fake Factor Method Applied to Low- $p_T$ Di-lepton Events . . . . .	26
6.3.1	Anti-identified Lepton Definitions . . . . .	27
6.3.2	Fake Lepton Composition . . . . .	32
6.3.3	Fake Factor Measurement . . . . .	40
6.4	Conclusion . . . . .	57
<b>7</b>	<b>Backgrounds</b>	<b>58</b>
7.1	Fake Lepton Background . . . . .	58
7.2	$t\bar{t}$ Background . . . . .	58
7.3	Drell-Yan Background . . . . .	58
7.4	Z+jets Background . . . . .	60
<b>8</b>	<b>Systematic Uncertainties</b>	<b>70</b>
8.1	Experimental . . . . .	70
8.2	Theoretical . . . . .	70
<b>9</b>	<b>Statistical Analysis</b>	<b>75</b>
<b>10</b>	<b>Results</b>	<b>76</b>
10.1	Compressed Higgsino . . . . .	77
10.2	Compressed Slepton . . . . .	78
<b>11</b>	<b>Conclusion</b>	<b>80</b>



# List of Figures

4.1	Kinematic distributions of signal samples . . . . .	10
4.2	Kinematic distributions of signal samples . . . . .	11
4.3	Trigger Efficiency as a function of MET after event preselection (left) and in a signal region similar to the analysis signal region (right) . . . . .	13
4.4	Trigger efficiency as a function of MET for the combined single muon trigger (left) and the combined dimuon trigger (right) . . . . .	13
5.1	Dilepton $\Delta R$ distribution before LepIsoCorrection (top) and after Lep- IsoCorrection (bottom) for the $ee$ -channel (left) and $\mu\mu$ -channel (right). . . . .	15
5.2	Dilepton invariant mass distribution before LepIsoCorrection (top) and after LepIsoCorrection (bottom) for the $ee$ -channel (left) and $\mu\mu$ -channel (right). . . . .	16
5.3	(left) Impact of the <code>NearbyLepIsoCorrection</code> tool on the efficiency of low-mass dilepton pairs in data. The data are shown in a region with $\Delta\phi(E_T^{\text{miss}}, p_t^{j1}) < 1.5$ to avoid the signal region. Events are triggered with the inclusive- $E_T^{\text{miss}}$ trigger. The red trend shows events with two baseline leptons without applying any isolation; the green shows the impact of applying <code>GradientLoose</code> isolation; the blue shows the result of the <code>NearbyLepIsoCorrection</code> applied to the <code>GradientLoose</code> sample. (right) Impact of the correction on a Higgsino LSP signal sample with $\Delta m(\chi, \chi) = 3 \text{ GeV}$ . . . . .	17
5.4	Comparison of Higgsino N2C1p (solid) and slepton (dashed) signals in the $R_{\ell\ell}$ variable for 10 GeV (dark) and 20 GeV (light) mass splittings. The $E_T^{\text{miss}}$ here acts as a proxy for the boost of the system. Only a 2 signal lepton selection is applied. . . . .	18
5.5	Distributions of $E_T^{\text{miss}}/H_T^{\text{leptons}}$ for the Higgsino (left) and Slepton (right) selections, after applying all signal region cuts except those on the $E_T^{\text{miss}}/H_T^{\text{leptons}}$ , $m_{ll}$ , and $m_{T2}$ . The black dashed line indicates the cut applied in the sig- nal region; events in the region below the black line are rejected. . . . .	19
5.6	Schematic illustrating the fully leptonic ( $Z \rightarrow \tau\tau$ ) + jets system moti- vating the construction of $m_{\tau\tau}$ . . . . .	19

5.7	Non-normalized cutflow with significance plot, showing how the significance for signal improves as more cuts are added. . . . .	20
6.1	Electron identification efficiency . . . . .	23
6.2	Schematic illustrating the fake factor method to estimate the fake lepton contribution in the signal region. . . . .	25
6.3	Fake electron composition as a function of $m_T$ for events in the full $m_T$ range (left) and as a function of $E_T^{\text{miss}}$ (top) for events in the range $m_T < 40 \text{ GeV}$ . . . . .	28
6.4	Fake electron composition as a function of denominator electron $p_T$ (left) and as a function of denominator electron $\eta$ (top) for events with $m_T < 40 \text{ GeV}$ . . . . .	28
6.5	Anti-ID muon composition in events with exactly zero $b$ -jets (top) and one or more $b$ -jets (bottom) as a function of $m_T$ (left) and as a function of $E_T^{\text{miss}}$ (right) The $E_T^{\text{miss}}$ distribution corresponds to events with $m_T < 40 \text{ GeV}$ . . . . .	30
6.6	Anti-ID muon composition in events with exactly zero $b$ -jets (top) and one or more $b$ -jets (bottom) as a function of denominator muon $p_T$ (left) and as a function of denominator muon $\eta$ (right) for events with $m_T < 40 \text{ GeV}$ . . . . .	31
6.7	Fake lepton composition as a function of leading and subleading lepton $p_T$ , with and without prompt (“Isolated” plus “ $\text{lep} \rightarrow \text{gamma} \rightarrow \text{lep}$ ”) leptons, for opposite sign electron pairs in the signal region. . . . .	32
6.8	Fake lepton composition as a function of leading and subleading lepton $p_T$ , with and without prompt (“Isolated” plus “ $\text{lep} \rightarrow \text{gamma} \rightarrow \text{lep}$ ”) leptons, for opposite sign muon pairs in the signal region. . . . .	33
6.9	Fake lepton composition as a function of leading and subleading lepton $p_T$ , with and without prompt (“Isolated” plus “ $\text{lep} \rightarrow \text{gamma} \rightarrow \text{lep}$ ”) leptons, for opposite sign electron pairs in the fake lepton control region. . . . .	34
6.10	Fake lepton composition as a function of leading and subleading lepton $p_T$ , with and without prompt (“Isolated” plus “ $\text{lep} \rightarrow \text{gamma} \rightarrow \text{lep}$ ”) leptons, for opposite sign muon pairs in the fake lepton control region. . . . .	35
6.11	Fake lepton composition as a function of leading and subleading lepton $p_T$ , with and without prompt (“Isolated” plus “ $\text{lep} \rightarrow \text{gamma} \rightarrow \text{lep}$ ”) leptons, for same sign electron pairs in the signal region. . . . .	36
6.12	Fake lepton composition as a function of leading and subleading lepton $p_T$ , with and without prompt (“Isolated” plus “ $\text{lep} \rightarrow \text{gamma} \rightarrow \text{lep}$ ”) leptons, for same sign muon pairs in the signal region. . . . .	37
6.13	Fake lepton composition as a function of leading and subleading lepton $p_T$ , with and without prompt (“Isolated” plus “ $\text{lep} \rightarrow \text{gamma} \rightarrow \text{lep}$ ”) leptons, for same sign electron pairs in the fake lepton control region. . . . .	38
6.14	Fake lepton composition as a function of leading and subleading lepton $p_T$ , with and without prompt (“Isolated” plus “ $\text{lep} \rightarrow \text{gamma} \rightarrow \text{lep}$ ”) leptons, for same sign muon pairs in the fake lepton control region. . . . .	39

6.15	The $E_T^{\text{miss}}$ (left) and $m_T$ (right) distributions for numerator (top) and denominator (bottom) electrons in the pre-scaled single-lepton-trigger sample. MC has been scaled to the data in the $E_T^{\text{miss}} > 200$ GeV region.	41
6.16	Electron $p_T$ for numerator (left) and denominator (right) objects in the pre-scaled single-lepton-trigger sample for events with $m_T < 40$ GeV. MC has been scaled to the data in the $E_T^{\text{miss}} > 200$ GeV region. . . . .	41
6.17	The numerator electron (left) and denominator electron (right) $p_T$ distributions for pre-scaled single-lepton-trigger, normalized to $1 \text{ pb}^{-1}$ . Blue curve: HLT_e5_lvhloose, red curve: HLT_e10_lvhloose_L1EM7, purple curve: HLT_e15_lvhloose_L1EM13, green curve: HLT_e20_lvhloose. . . .	42
6.18	Electron fake factors <i>before</i> requiring a hard jet of $p_T > 100$ GeV, computed from single-electron prescaled triggers as a function of electron $p_T$ (left) and leading jet $p_T$ (right). Fake factors for electron $p_T$ 4.5 – 5 GeV are taken to be the same as electron $p_T$ 5 – 6 GeV. A red line denotes the average electron fake factor over all electron $p_T$ of 0.267. . . . .	42
6.19	Electron fake factors computed from single-electron prescaled triggers as a function of electron $p_T$ (left) and electron $\eta$ (right) in the kinematic region with leading jet $p_T > 100$ GeV. Fake factors for electron $p_T$ 4.5 – 5 GeV are taken to be the same as electron $p_T$ 5 – 6 GeV. A red line denotes the average electron fake factor over all electron $p_T$ of 0.211. . . . .	43
6.20	Electron fake factors computed from single-electron prescaled triggers as a function of leading jet $p_T$ (left) and $\Delta\phi_{\text{jet}-E_T^{\text{miss}}}$ (right). A red line denotes the average electron fake factor over all electron $p_T$ of 0.211. . . .	44
6.21	Electron fake factors computed from single-electron prescaled triggers as a function of the jet multiplicity (left) and the $b$ -jet multiplicity (right). A red line denotes the average electron fake factor over all electron $p_T$ of 0.211. . . . .	44
6.22	Electron fake factors computed from single-electron prescaled triggers as a function of the average interaction per bunch crossing (left) and the number of primary vertices (right). A red line denotes the average electron fake factor over all electron $p_T$ of 0.211. . . . .	45
6.23	Relative uncertainties on electron fake factors binned electron $p_T$ . . . . .	45
6.24	The $E_T^{\text{miss}}$ (left) and $m_T$ (right) distributions for numerator (top) and denominator (bottom) muons in the prescaled single-lepton-trigger sample for events with exactly zero $b$ -jets. MC has been scaled to the data in the $E_T^{\text{miss}} > 200$ GeV region. . . . .	48
6.25	The $E_T^{\text{miss}}$ (left) and $m_T$ (right) distributions for numerator (top) and denominator (bottom) muons in the prescaled single-lepton-trigger sample for events with one or more $b$ -jets. MC has been scaled to the data in the $E_T^{\text{miss}} > 200$ GeV region. . . . .	49

6.26 Muon $p_T$ for numerator (left) and denominator (right) objects in the prescaled single-muon trigger sample for events with $m_T < 40 \text{ GeV}$ . MC has been scaled to the data in the $m_T > 100 \text{ GeV}$ region. Distributions from [?]. . . . .	49
6.27 Muon $p_T$ for numerator (left) and denominator (right) objects in the prescaled single-muon trigger sample for events with $m_T < 40 \text{ GeV}$ . MC has been scaled to the data in the $m_T > 100 \text{ GeV}$ region. Distributions from [?]. . . . .	50
6.28 The numerator muon (left) and denominator denominator (right) $p_T$ distributions for prescaled single-muon triggers, normalized to $1 \text{ pb}^{-1}$ . Blue curve: HLT_mu4, red curve: HLT_mu10, purple curve: HLT_mu14, green curve: HLT_mu18. . . . .	50
6.29 Muon fake factors <i>before</i> requiring a hard jet of $p_T > 100 \text{ GeV}$ , computed from single-muon prescaled triggers as a function of muon $p_T$ (top-left), as a function of leading jep $p_T$ (top-right), and as a function of $b$ -jet multiplicity (bottom). A red line denotes the average muon fake factor over all muon $p_T$ . . . . .	52
6.30 Muon fake factors computed from single-muon prescaled triggers as a function of muon $p_T$ in events with exactly zero $b$ -jets (left) and one or more $b$ -jets (right). A red line denotes the average muon fake factor over all muon $p_T$ . . . . .	53
6.31 Muon fake factors computed from single-muon prescaled triggers as a function of muon $\eta$ in events with exactly zero $b$ -jets (left) and one or more $b$ -jets (right). A red line denotes the average muon fake factor over all muon $p_T$ . . . . .	54
6.32 Muon fake factors computed from single-muon prescaled triggers as a function of $\Delta\phi_{jet-E_T^{\text{miss}}}$ in events with exactly zero $b$ -jets (left) and one or more $b$ -jets (right). A red line denotes the average muon fake factor over all muon $p_T$ . . . . .	54
6.33 Muon fake factors computed from single-muon prescaled triggers as a function of the jet multiplicity in events with exactly zero $b$ -jets (left) and one or more $b$ -jets (right). A red line denotes the average muon fake factor over all muon $p_T$ . . . . .	55
6.34 Muon fake factors computed from single-muon prescaled triggers as a function of the average number of interactions per bunch crossing in events with exactly zero $b$ -jets (left) and one or more $b$ -jets (right). A red line denotes the average muon fake factor over all muon $p_T$ . . . . .	55
6.35 Muon fake factors computed from single-muon prescaled triggers as a function of the number of primary vertices in events with exactly zero $b$ -jets (left) and one or more $b$ -jets (right). A red line denotes the average muon fake factor over all muon $p_T$ . . . . .	56
6.36 Relative uncertainties on muon fake factors versus muon $p_T$ in zero $b$ -jets bin (left) and one or more $b$ -jets bin (right). . . . .	56

7.1	Data events passing inclusive $E_T^{\text{miss}}$ triggers with opposite sign baseline leptons in the dilepton invariant mass $m_{\ell\ell}$ spectrum. The $\Delta\phi(j_1, \mathbf{p}_T^{\text{miss}})$ variable is inverted to ensure this is orthogonal to the signal region. . . . .	59
7.2	CR-top $ee + \mu\mu + e\mu + \mu e$ channel, pre-fit distributions. . . . .	61
7.3	$m_T^{\ell_1} + m_T^{\ell_2}$ . . . . .	62
7.4	CR-top $ee + \mu\mu + e\mu + \mu e$ channel, pre-fit distributions. . . . .	62
7.5	$m_{T2}^{100}$ . . . . .	63
7.6	CR-top $ee + \mu\mu + e\mu + \mu e$ channel, pre-fit distributions. . . . .	63
7.7	CR-tau $ee + \mu\mu + e\mu + \mu e$ channel, pre-fit distributions. . . . .	64
7.8	CR-tau $ee + \mu\mu + e\mu + \mu e$ channel, pre-fit distributions. . . . .	65
7.9	CR-tau $ee + \mu\mu + e\mu + \mu e$ channel, pre-fit distributions. . . . .	66
7.10	VR-VV $ee + \mu\mu + e\mu + \mu e$ channel, pre-fit distributions. . . . .	67
7.11	VR-VV $ee + \mu\mu + e\mu + \mu e$ channel, pre-fit distributions. . . . .	68
7.12	VR-VV $ee + \mu\mu + e\mu + \mu e$ channel, pre-fit distributions. . . . .	69
8.1	QCD scale, $\alpha_s$ and PDF uncertainties on the shape and normalization of the diboson background in the Higgsino and slepton signal regions (with no lepton flavor requirement). . . . .	71
8.2	QCD scale, $\alpha_s$ and PDF uncertainties on the shape and normalization of the $Z \rightarrow \tau\tau$ background in the Higgsino and slepton signal regions (with no lepton flavor requirement). . . . .	72
8.3	QCD scale and PDF uncertainties on the shape and normalization of the $t\bar{t}$ background in the Higgsino and slepton signal regions (with no lepton flavour requirement). . . . .	73
8.4	Comparison of the $m_{\ell\ell}$ (left) and $m_{T2}$ (right) shapes predicted by different $t\bar{t}$ (top) and $VV$ (bottom) MC generators, in the Higgsino and slepton signal regions. All distributions are normalized to the same number of entries. The gray band displayed in the ratio pad under each distribution represents the modeling uncertainty assigned to each background in each of the bins. . . . .	74
10.1	Summary of Monte Carlo yields in control, validation and signal regions in a background-only fit using data only in the two CRs to constrain the fit. . . . .	77
10.2	Expected 95% CL exclusion sensitivity (blue dashed line) with $\pm 1\sigma_{\text{exp}}$ (yellow band) from experimental systematics and observed limits (red solid) with $\pm 1\sigma_{\text{theory}}$ (dotted red) from signal cross section uncertainties. A shape fit of Higgsino signals to the $m_{\ell\ell}$ spectrum is used to derive the limit is displayed in the $m(\tilde{\chi}_2^0) - m(\tilde{\chi}_1^0)$ vs $m(\tilde{\chi}_2^0)$ plane. The chargino $\tilde{\chi}_1^\pm$ mass is assumed to be half way between the two lightest neutralinos. The grey region denotes the lower chargino mass limit from LEP [?]. . . . .	78

- 10.3 Expected 95% CL exclusion sensitivity (blue dashed line) with  $\pm 1\sigma_{\text{exp}}$  (yellow band) from experimental systematics and observed limits (red solid) with  $\pm 1\sigma_{\text{theory}}$  (dotted red) from signal cross section uncertainties. A shape fit of slepton signals to the  $m_{\text{T}2}^{100}$  spectrum is used to derive the limit projected into the  $m(\tilde{\ell}) - m(\tilde{\chi}_1^0)$  vs  $m(\tilde{\ell})$  plane. The slepton  $\tilde{\ell}$  refers to a 4-fold mass degenerate system of left- and right-handed selectron and smuon. The grey region denotes a conservative right-handed smuon  $\tilde{\mu}_R$  mass limit from LEP [?], while the blue region is the 4-fold mass degenerate slepton limit from ATLAS Run 1 [?]. . . . .

# List of Tables

6.1	Pre-scaled single-lepton triggers from 2015 and 2016 used to compute the lepton fake factors. The pre-scaled luminosities shown are taken from LumiCalc. . . . .	26
6.2	Summary of signal electron definitions. . . . .	27
6.3	Summary of anti-ID electron definitions. . . . .	28
6.4	Summary of signal muon definitions. . . . .	29
6.5	Summary of anti-ID muon definitions. . . . .	29
6.6	Single-Electron triggers used for fake factor computation and their corresponding $p_T$ range. . . . .	40
6.7	Single-muon triggers used for fake factor computation and their corresponding $p_T$ range. . . . .	51

## Abstract

Searches for Electroweak Production of Compressed Supersymmetry in Events  
with Soft Leptons Plus Missing Transverse Momentum and Hard Jet Recoil

by

Sheena Calie Schier

Supersymmetry (SUSY) is an extension of the Standard Model that predicts a boson (fermion) partner for each fermion (boson) in the Standard Model. Weak scale SUSY is attractive for reasons like improving gauge coupling unification, reducing fine-tuning in the Higgs sector and providing a dark matter candidate. In this thesis, I present a dedicated search for direct production of new colorless weak scale states in a compressed mass spectra with final states characterized by soft visible decay products. This analysis uses  $pp$  collisions at  $\sqrt{s} = 13$  TeV at the Large Hadron Collider and collected by the ATLAS experiment during 2015 and 2016 corresponding to  $36.1\text{ fb}^{-1}$  of integrated luminosity. This analysis selects events with two soft electrons or muons and missing transverse momentum ( $E_T^{miss}$ ) recoiling against hadronic initial state radiation. Backgrounds from  $t\bar{t}$ , diboson, and other production mechanisms with prompt leptons are estimated with Monte Carlo simulation while reducible backgrounds with instrumental  $E_T^{miss}$  and fake/non-prompt leptons is estimated with a mix of Monte Carlo and data-driven methods. Results are consistent with Standard Model expectation and limits on compressed supersymmetric states are extended for the first time since LEP.

To my father,

Lecil Charles Schier,

the person who taught me at the age of 7 that the grass in not green.

## **Acknowledgments**

I want to “thank” my committee, without whose ridiculous demands, I would have graduated so, so, very much faster.

## **Part I**

### **First Part**

# Chapter 1

## Introduction

Particle accelerators have been around since such and such time and have been the source of the most precise physics measurements and lead to deeper understanding of the most fundamental forces and particles in nature. Discovery of top quarks at this collider and the W and Z bosons. Da da da LEP  $e^+e^-$  machine blah blah. The Large Hadron Collider pushing into unseen energy realms has the imminent task of finding the Higgs boson, but that is not all. There must be more, and it was believed for decades new physics was right around the corner from LEP(and others).

# Chapter 2

## The Standard Model of Particle Physics and Additional Theories

The universe seems like a very complex place made out of many types of material that interacts by various complex mechanisms. Although this will always remain true, particle physics has constructed a theory that incorporates all fundamental particles and explains their existence and interactions in simplicity through the field equations that describe the fundamental forces in the universe. This theory is called the Standard Model of Particle Physics and, apart from the absence of gravity which is far too weak to be described by particle interactions, is fundamentally complete.

### 2.1 Forces and Particles

The Standard Model describes three of the four known fundamental forces or our universe; electromagnetic force, the strong force, and the weak force. It leaves

out the gravitational force only because the energy scale at which gravity does its business is so many orders of magnitude below the other forces that there are intrinsic incompatibilities in their description of particle interactions. According to experiment, there are only a hand full of fundamental particles, among which can be separated into two distinct categories: fermions and bosons. These two types of particles play completely different roles in the state and phenomena of the universe. [?]

You and I and the entire world we experience is comprised of fermions, spin  $\frac{1}{2}$  Dirac particles, that can be further categorized as leptons and quarks depending on their intrinsic propensity to interact with a given fundamental force field or not. The lepton family consists of three types of electron ( $e, \mu, \tau$ ) and their associated neutrino partners ( $\nu_e, \nu_\mu, \nu_\tau$ ).

## 2.2 Mathematical Formalism of the Standard Model

Field equations and fermion and boson interactions.

## 2.3 Gauge Symmetries and Spontaneous Symmetry Breaking

ing

$$U(1)_Y \times SU(2)_L \times SU(3)_S$$

## **2.4 Higgs Mechanism and Gauge Boson Masses**

Explain local SU(2) gauge symmetry breaking, the production of the Higgs boson and how this allows for massive weakly interacting gauge bosons.

## **2.5 Shortcomings of the Standard Model**

### **2.5.1 Darkmatter**

One alarming problem with the Standard Model is its incapability to explain dark matter.

## **2.6 Supersymmetry**

Extension of the Poincare Group which leads to boson-fermion symmetry.

## **2.7 Phenomenology of Direct Production of Higgsinos and Sleptons in Compressed Scenarios**

Here talk about the discriminating variables for the higgsino and slepton signal regions (mll and mt2).

# **Chapter 3**

## **ATLAS Experiment**

The Large Hadron Collider (LHC) is a 27 km long circular proton accelerator with proton beams moving in opposite directions around the ring at speeds near 99.99% the speed of light. The beams travel around the ring in separate vacuum beam pipes and are accelerated and directed around the ring using gigantic semi-conducting magnets. To reach LHC energies the proton beams are accelerated in smaller accelerator structures gradually increasing in size until they are injected into the LHC, which is still the largest and most powerful accelerator in the world. The beams are made to collide at 4 different interaction points at which there are 4 different detector experiments: ALICE, LHC-B, CMS, and ATLAS.

## **3.1 Tracking**

### **3.1.1 Pixel Detector**

Inner most pixelated tracker.

### **3.1.2 Semi-Conductor Tracker**

Middle silicon strip tracker.

### **3.1.3 Transition Radiation Tracker**

Outer most straw tube tracker.

## **3.2 Calorimetry**

### **3.2.1 Electromagnetic Calorimeter**

Measures energy of electromagnetic objects.

### **3.2.2 Hadronic Calorimeter**

Measures energy of hadronic objects

## **3.3 Muon System**

An outer tracker dedicated entirely to tracking muons.

### **3.4 DAQ and Trigger**

Complex computing system to acquire and store data.

# Chapter 4

## MC and Data samples

Can talk about integrated lumi and maybe event weight

The event weights are very important. Currently I am applying the total weight as:

$$totalWeight = ttbarNNLOWeight * pileupWeight * eventWeight * leptonWeight * jvtWeight * bTagWeight \quad (4.1)$$

The weights are recalculated during the merging phase using the cross-section and the sumOfWeightsHist.

### 4.1 Signal Samples

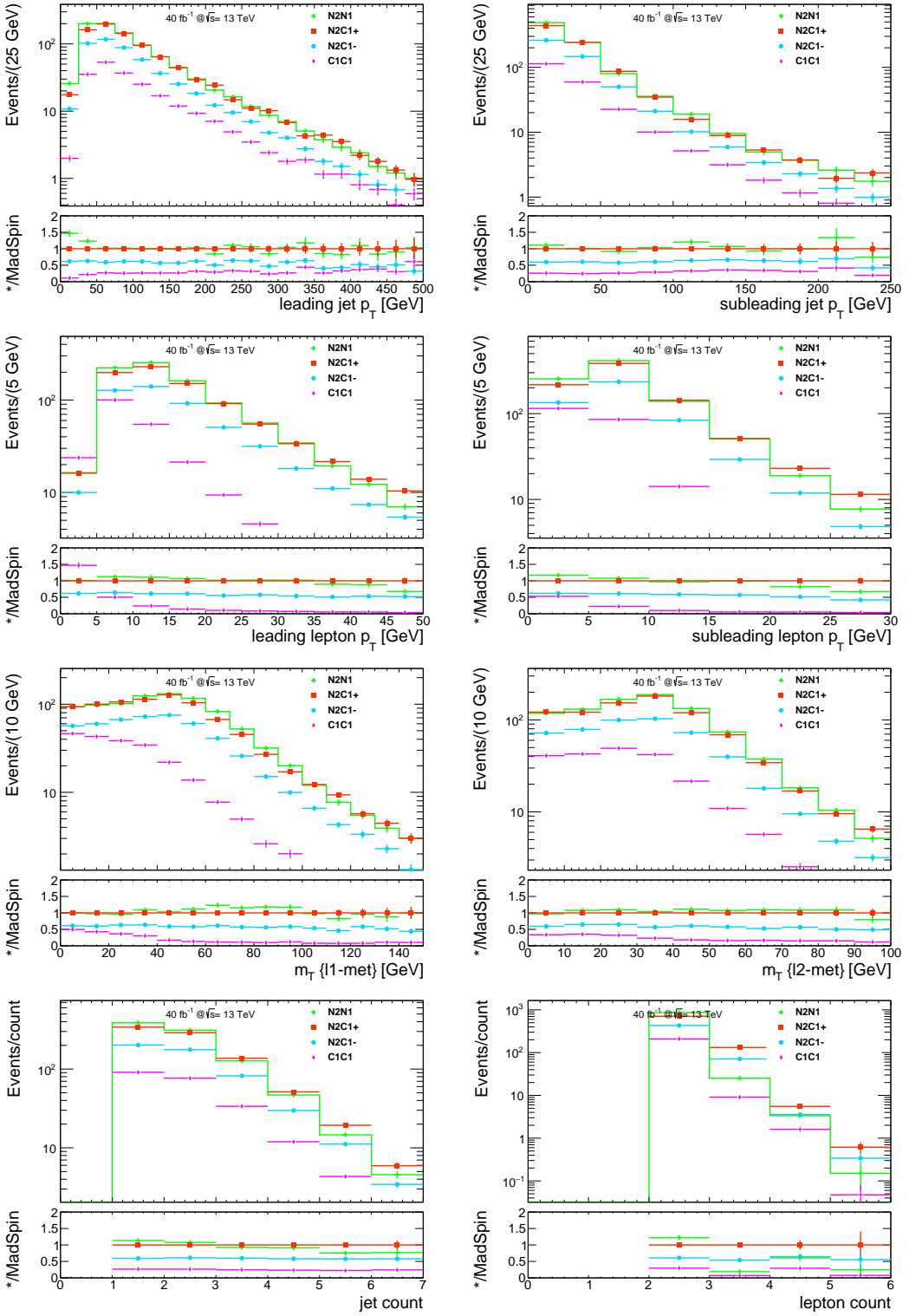


Figure 4.1: Kinematic distributions of signal samples

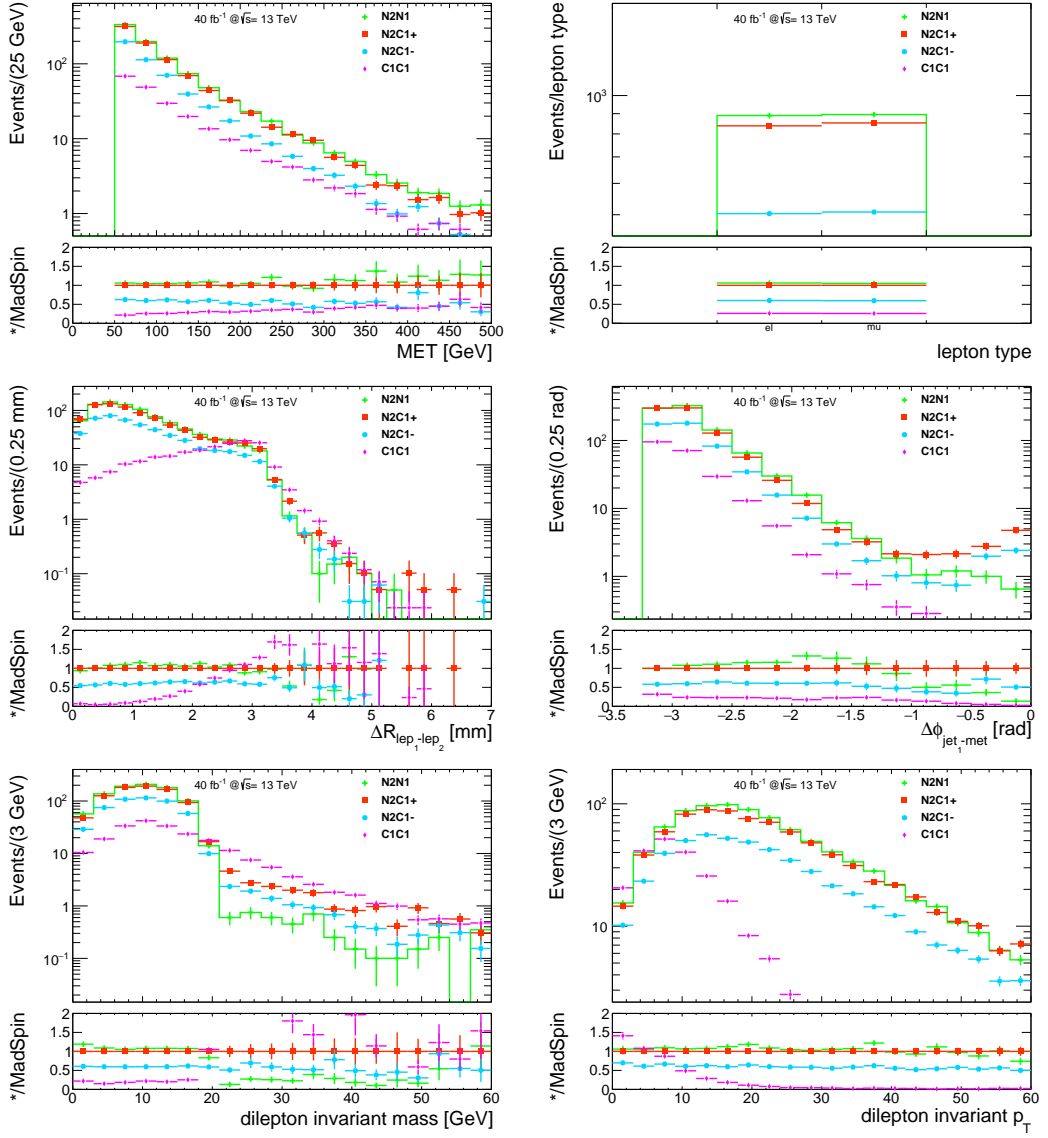


Figure 4.2: Kinematic distributions of signal samples

## **4.2 Triggers**

### **4.2.1 MET Triggers**

Inclusive met trigger efficiencies

### **4.2.2 Combined Triggers**

Lepton plus jet plus met trigger efficiencies..

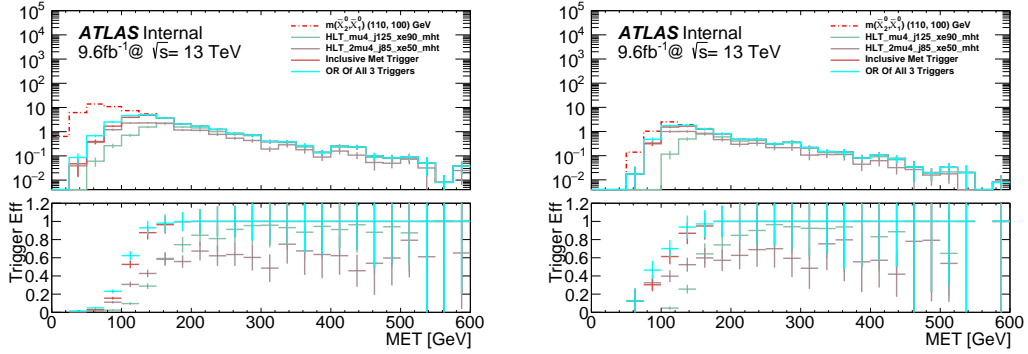


Figure 4.3: Trigger Efficiency as a function of MET after event preselection (left) and in a signal region similar to the analysis signal region (right)

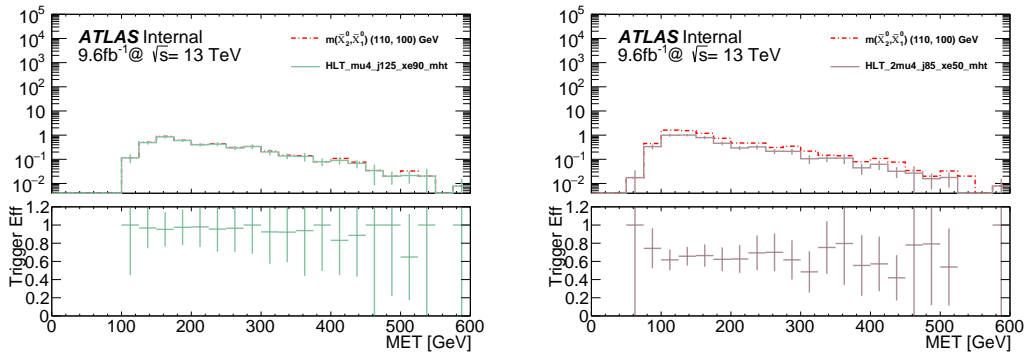


Figure 4.4: Trigger efficiency as a function of MET for the combined single muon trigger (left) and the combined dimuon trigger (right)

# Chapter 5

## Event Selection and Signal Regions

Study signal MonteCarlos samples to understand the phenomenology of compressed higgsino and slepton production during and LHC collision and subsequent decay in the ALTAS detector. These studies inform our choices choices for signal region cuts for the slepton and higgsino searches.

### 5.1 Object Definitions

Electrons, muons, jets, photons, met, overlap removal, isolation for nearby leptons.. (lepton truth matching?)

### 5.2 Discriminating Variables

$E_T^{\text{miss}}$ , d phi j-met, min d phi jets-met,  $p_T(j_i)$ , Number of  $b$ -tagged jets  $N_{b\text{-jets}}$   
Same flavour lepton pair with opposite charge,  $\Delta R_{\ell\ell}$ ,  $m_{\ell\ell}$ ,  $m_{T2}^{m_\chi}, m_T^{\ell_1}$ ,  $E_T^{\text{miss}}/H_T^{\text{leptons}}$ ,

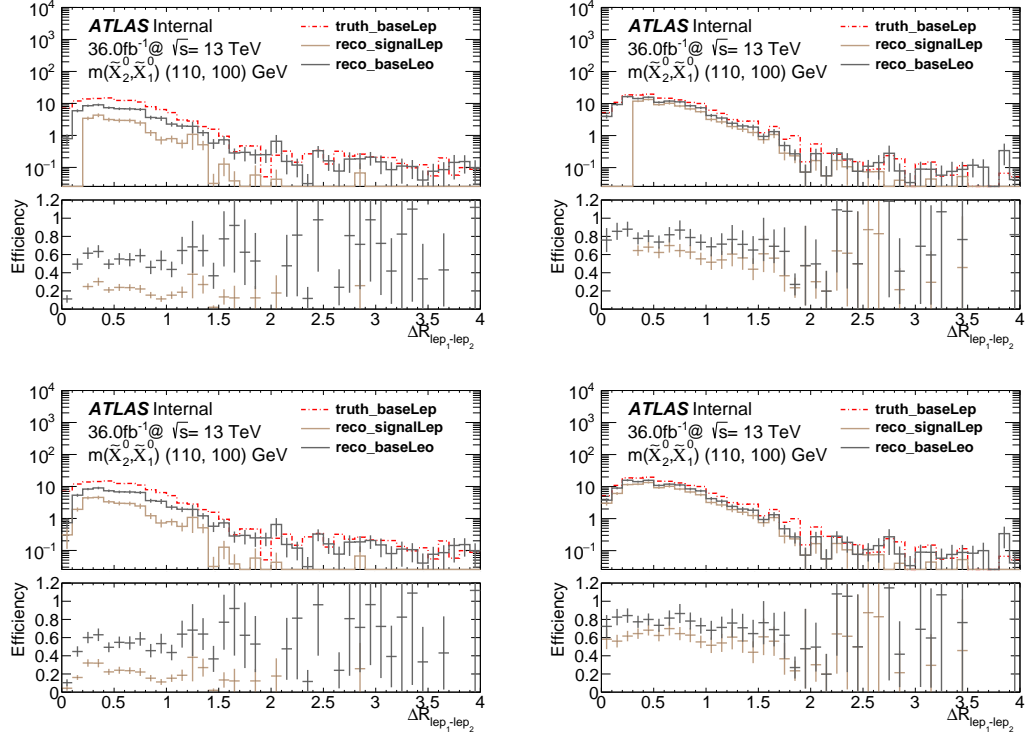


Figure 5.1: Dilepton  $\Delta R$  distribution before LepIsoCorrection (top) and after LepIso-Correction (bottom) for the  $ee$ -channel (left) and  $\mu\mu$ -channel (right).

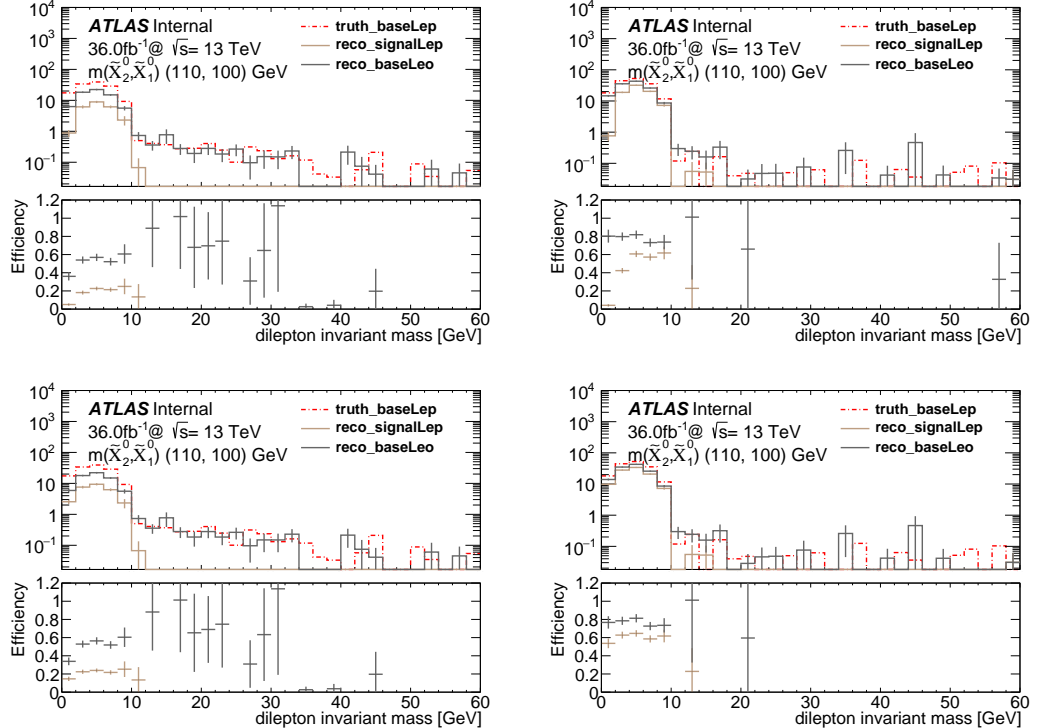


Figure 5.2: Dilepton invariant mass distribution before LepIsoCorrection (top) and after LepIsoCorrection (bottom) for the  $ee$ -channel (left) and  $\mu\mu$ -channel (right).

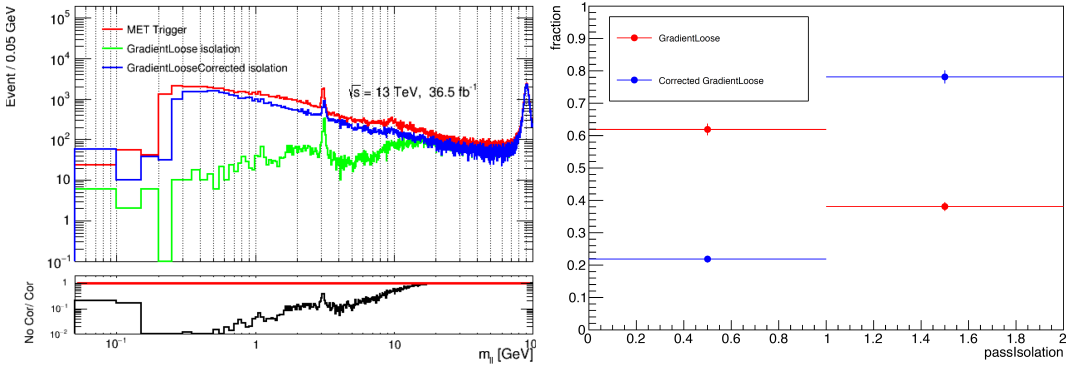


Figure 5.3: (left) Impact of the `NearbyLepIsoCorrection` tool on the efficiency of low-mass dilepton pairs in data. The data are shown in a region with  $\Delta\phi(E_T^{\text{miss}}, p_t^{j1}) < 1.5$  to avoid the signal region. Events are triggered with the inclusive- $E_T^{\text{miss}}$  trigger. The red trend shows events with two baseline leptons without applying any isolation; the green shows the impact of applying `GradientLoose` isolation; the blue shows the result of the `NearbyLepIsoCorrection` applied to the `GradientLoose` sample. (right) Impact of the correction on a Higgsino LSP signal sample with  $\Delta m(\chi, \chi) = 3$  GeV.

$m_{\tau\tau}$

### 5.2.1 Signal Regions

#### 5.2.2 Slepton Signal Regions

This signal region based on MT2 cuts

#### 5.2.3 Higgsino Signal Regions

This signal region based on Mll cuts

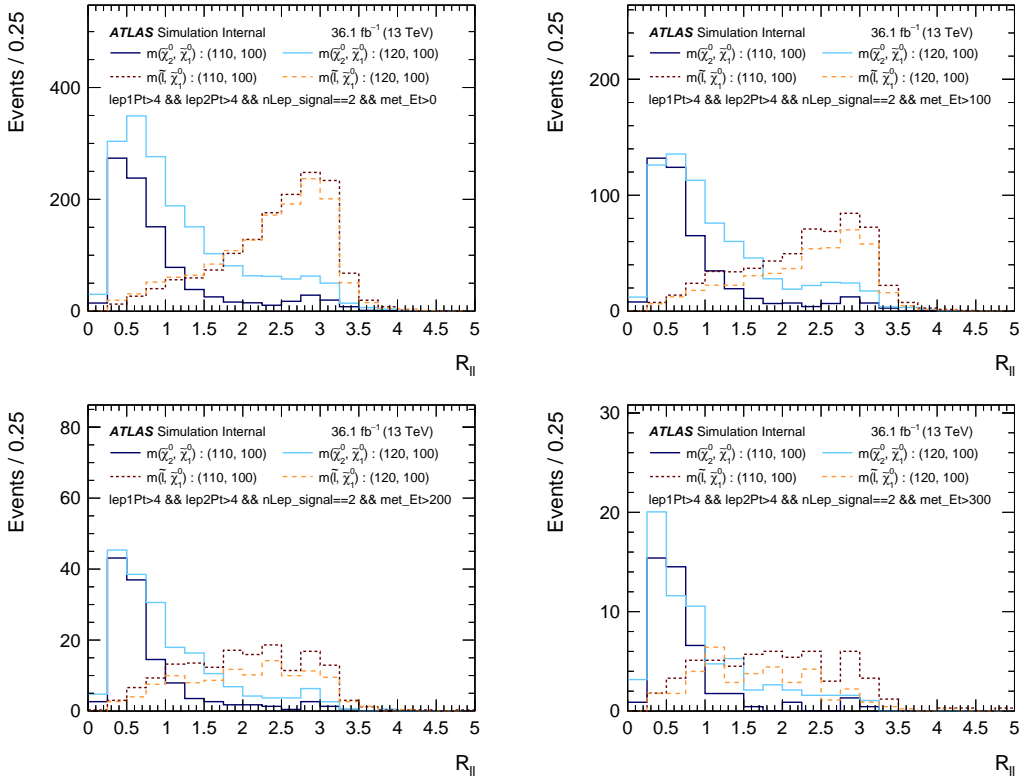


Figure 5.4: Comparison of Higgsino N2C1p (solid) and slepton (dashed) signals in the  $R_{\ell\ell}$  variable for 10 GeV (dark) and 20 GeV (light) mass splittings. The  $E_T^{\text{miss}}$  here acts as a proxy for the boost of the system. Only a 2 signal lepton selection is applied.

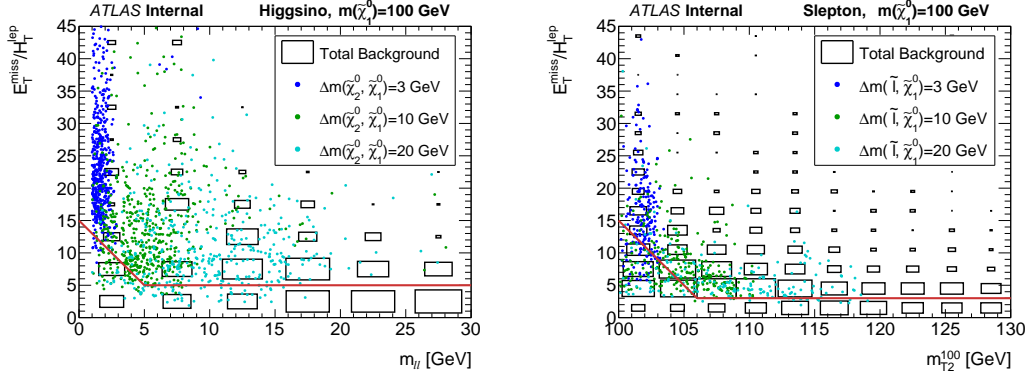


Figure 5.5: Distributions of  $E_T^{\text{miss}}/H_T^{\text{leptons}}$  for the Higgsino (left) and Slepton (right) selections, after applying all signal region cuts except those on the  $E_T^{\text{miss}}/H_T^{\text{leptons}}$ ,  $m_{ll}$ , and  $m_{T2}$ . The black dashed line indicates the cut applied in the signal region; events in the region below the black line are rejected.

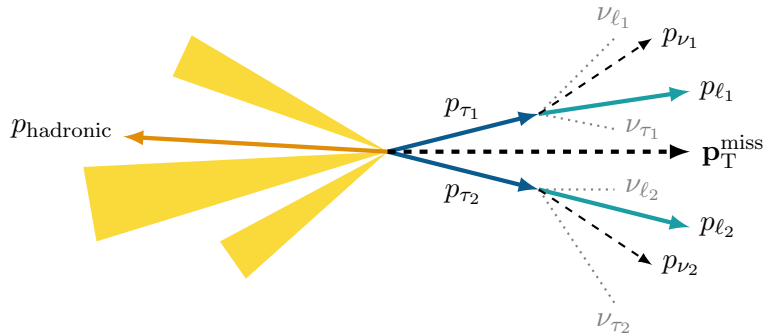


Figure 5.6: Schematic illustrating the fully leptonic ( $Z \rightarrow \tau\tau$ ) + jets system motivating the construction of  $m_{\tau\tau}$ .

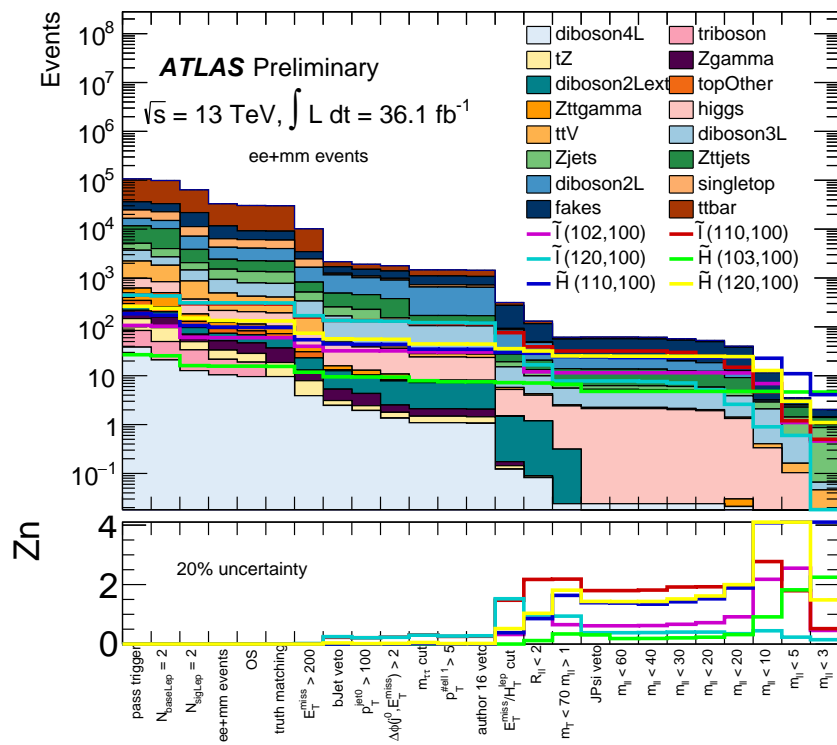


Figure 5.7: Non-normalized cutflow with significance plot, showing how the significance for signal improves as more cuts are added.

# Chapter 6

## Fake Factor Method

Backgrounds to beyond Standard Model physics signals mostly come from Standard Model physics processes that produce the same physics signals we are looking for. In that case, the goal is the estimate the rate of the background process and subtract it from the data so the new physics signal, if any, is all that remains. Another type of background can come from processes that should not produce the same final state as the signal process, and yet, because of mismeasurements inside the detector, can still mimic signal events. For low pt dilepton signals, this background is a dominant background and primarily comes from W+jets events where one jets is misidentified as a lepton. The best estimate of this background comes from data because MC simulation does not model the detector shortcomings that lead to these mismeasurements very well. The "fake factor" method is a data driven approach to modeling backgrounds from particle misidentification in the detector. (Explain the layout of the rest of the chapter)

- Introduction

- Description

- Application

- Conclusion

## 6.1 Introduction

- lepton identification and misidentification
- Compare production cross-sections of signal and W+jets processes
- Sources of electron and muon misidentification
- How to model backgrounds from misidentification (can't use MC, must choose data driven method)
- Concept of fake factor method
- Primary fake background is W+jets (multi-jet is minuscule... how do I qualify this?)
- Rest of chapter describes FF method in the context of my analysis

Efficient lepton identification techniques make leptons powerful discriminators in ATLAS physics searches with large background rejection and heavily suppressed QCD multi-jets. Jet suppression is very high in the range of lepton  $p_T > 20\text{GeV}$  but degrades at lower lepton  $p_T$ . Sources of misidentified electrons are charged hadrons, where a hadronic jet fakes an electron, or photon conversions and heavy-flavor decays, where

there is a true but non-prompt electron that is created inside the detector rather than at the primary vertex where true, prompt electrons are made.

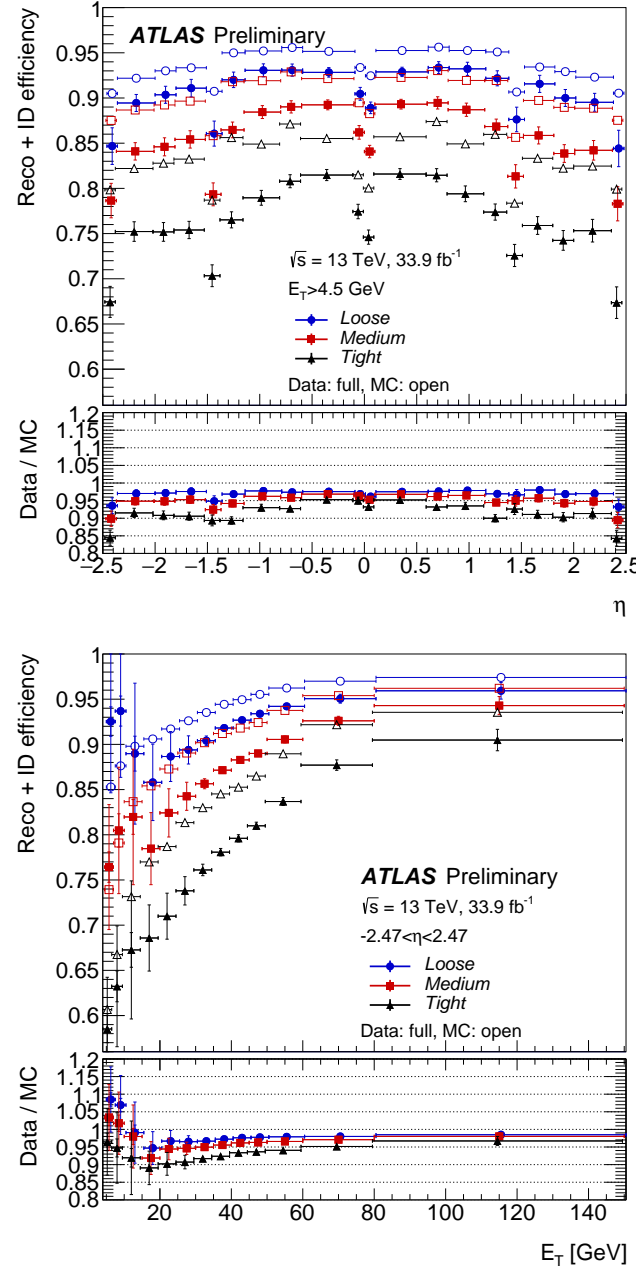


Figure 6.1: Electron identification efficiency

\*\*Make plot comparing production cross-sections, at least for W+jets and Higgsino/Slepton, and maybe even include other reducible background production cross-sections.

## 6.2 Description of Fake Factor Method

- General description of fake factor method (measurement in control region then extrapolated to signal region)
- We know what the signal region is already (described in Chapter ..)
- Control region, meant to select events with misidentified leptons, is defined by signal region cuts but with one lepton chosen to satisfy a selection criteria that is more likely to include more misidentified particles than that used in the analysis signal region. A control region designed to capture W+jets events where a jet is misidentified as a lepton would be the same as the signal region requiring two leptons, but only one lepton is defined as an analysis lepton, while the other has at least one orthogonal selection criteria cut that makes it easier to include jets in the container of lepton identified in this particular way.
- Electrons and muons are treated separately
- Fake factor is the ratio of leptons passing analysis lepton identification criteria to the leptons passing anti-identification criteria, measured in a region of kinematic phase space contrived to be enriched in fake leptons. This will be considered as

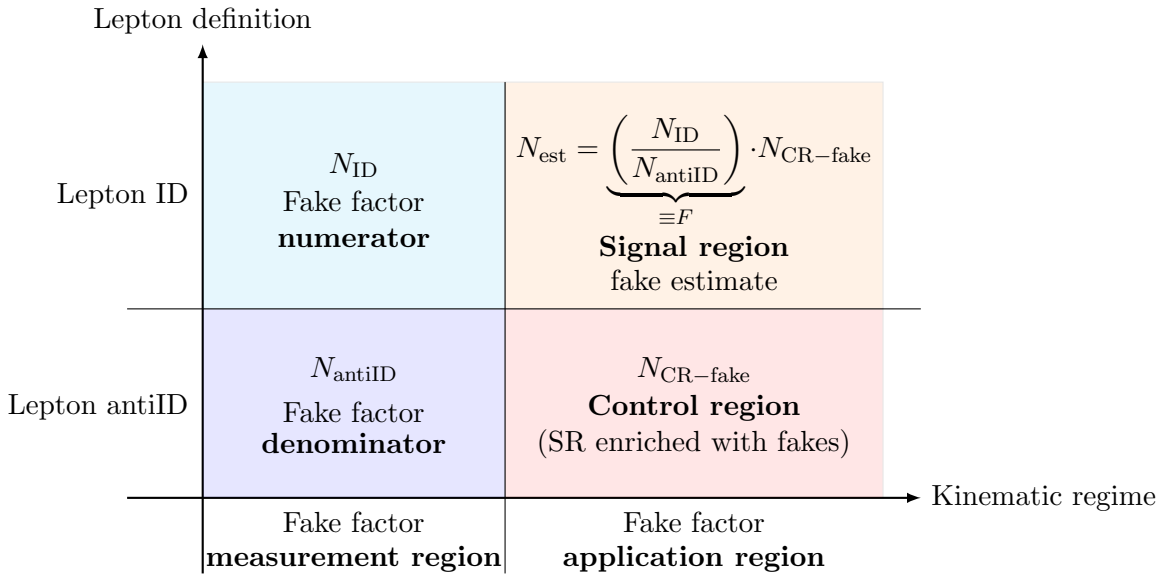


Figure 6.2: Schematic illustrating the fake factor method to estimate the fake lepton contribution in the signal region.

the fake factor measurement region in this thesis

- Fake background contribution estimated by scaling the number of selected events in the control region by the fake factor.
- Separate samples are used to measure the fake factor and count the number of events in the control region
- control region and anti-ID lepton definition have contamination from sources that are not from the background of interest

Explain signal and control regions as well as fake factor measurement and application regions.

The fake factors are computed from events with  $m_T < 40$  GeV, using the distributions in Fig. 6.16, as:

$$F(p_T) = \frac{\text{Numerator}_{\text{data}} - \text{Numerator}_{\text{MC}}}{\text{Denominator}_{\text{data}} - \text{Denominator}_{\text{MC}}} \quad (6.1)$$

### 6.3 Fake Factor Method Applied to Low- $p_T$ Di-lepton Events

- Describe data samples used for FF measurement
- Describe data samples used for fake background estimate

Trigger	Prescaled Luminosity [pb <sup>-1</sup> ]	
	2015	2016
HLT_e5_lhvloose	0.1	0.1
HLT_e10_lhvloose_L1EM7	0.5	0.8
HLT_e15_lhvloose_L1EM13VH	5.5	9
HLT_e20_lhvloose	10	17
HLT_mu4	0.5	0.5
HLT_mu10	2.3	2.5
HLT_mu14	25	14
HLT_mu18	26	48

Table 6.1: Pre-scaled single-lepton triggers from 2015 and 2016 used to compute the lepton fake factors. The pre-scaled luminosities shown are taken from `LumiCalc`.

### 6.3.1 Fake Lepton Composition

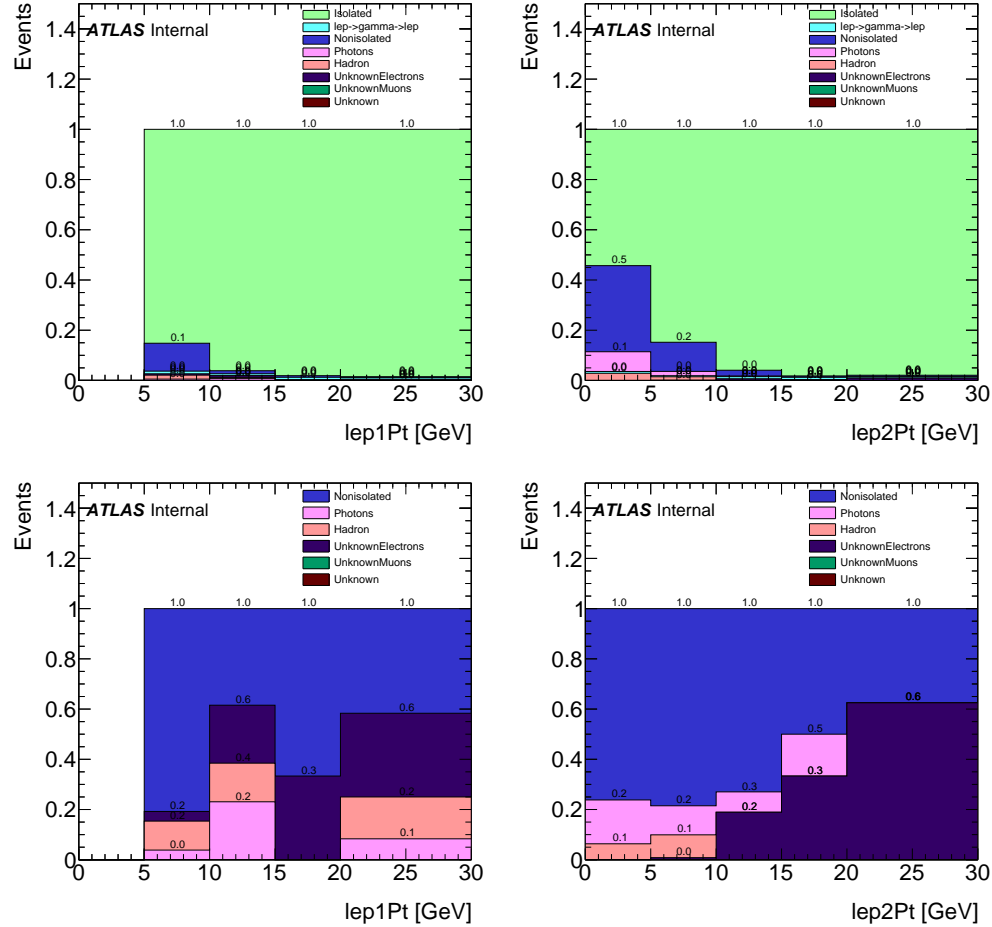


Figure 6.3: Fake lepton composition as a function of leading and subleading lepton  $p_T$ , with and without prompt (“Isolated” plus “ $\text{lep} \rightarrow \text{gamma} \rightarrow \text{lep}$ ”) leptons, for opposite sign electron pairs in the signal region.

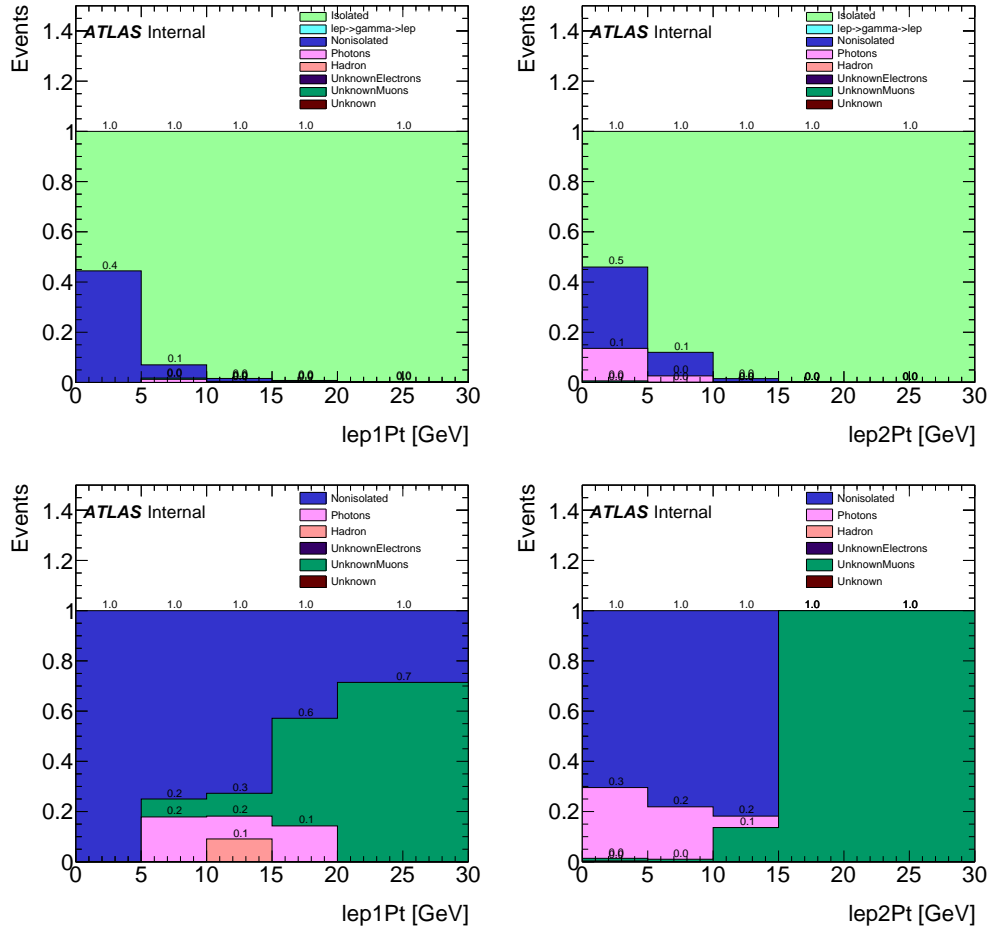


Figure 6.4: Fake lepton composition as a function of leading and subleading lepton  $p_T$ , with and without prompt (“Isolated” plus “ $\text{lep}\rightarrow\text{gamma}\rightarrow\text{lep}$ ”) leptons, for opposite sign muon pairs in the signal region.

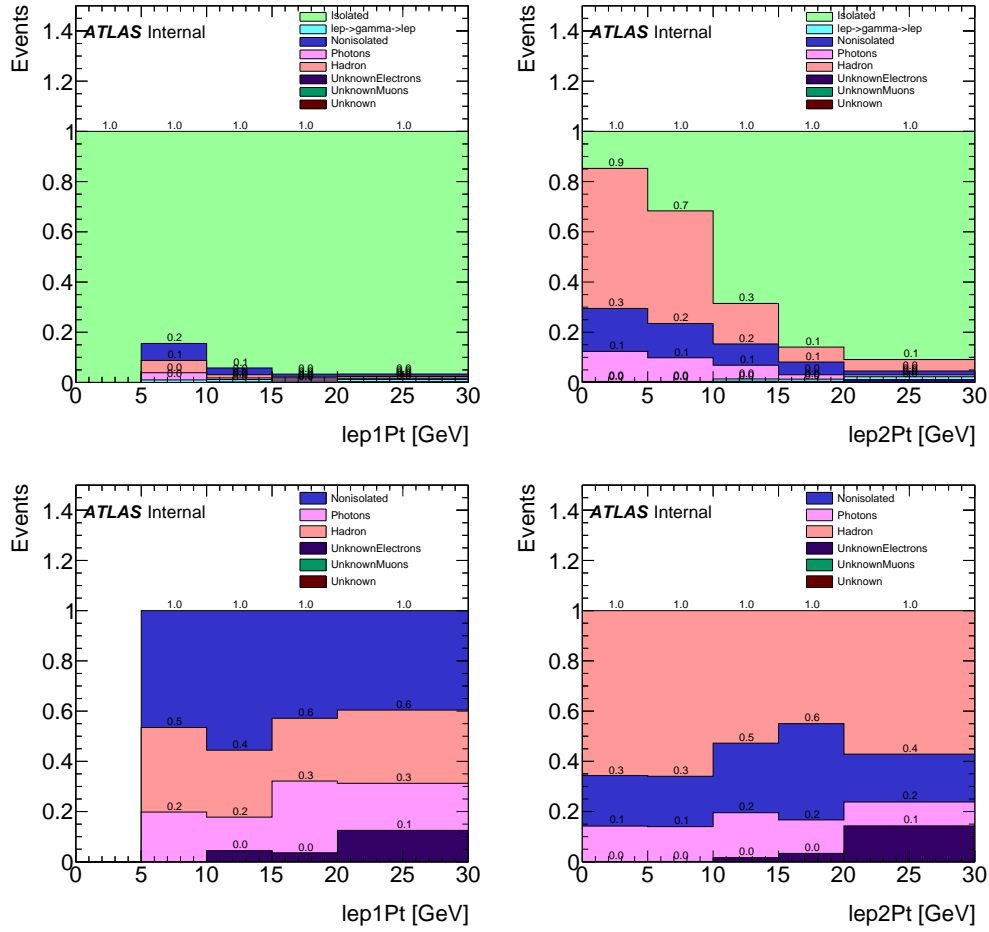


Figure 6.5: Fake lepton composition as a function of leading and subleading lepton  $p_T$ , with and without prompt (“Isolated” plus “lep $\rightarrow$ gamma $\rightarrow$ lep”) leptons, for opposite sign electron pairs in the fake lepton control region.

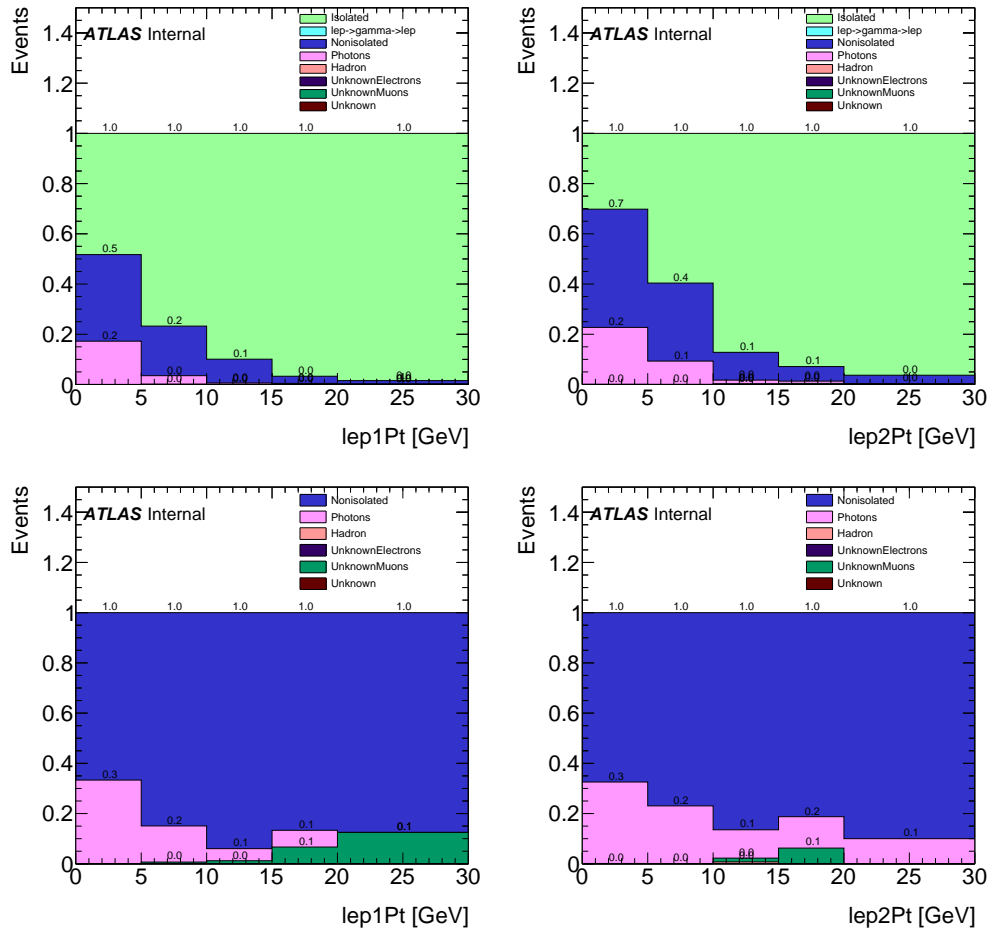


Figure 6.6: Fake lepton composition as a function of leading and subleading lepton  $p_T$ , with and without prompt (“Isolated” plus “lept $\rightarrow$ gamma $\rightarrow$ lept”) leptons, for opposite sign muon pairs in the fake lepton control region.

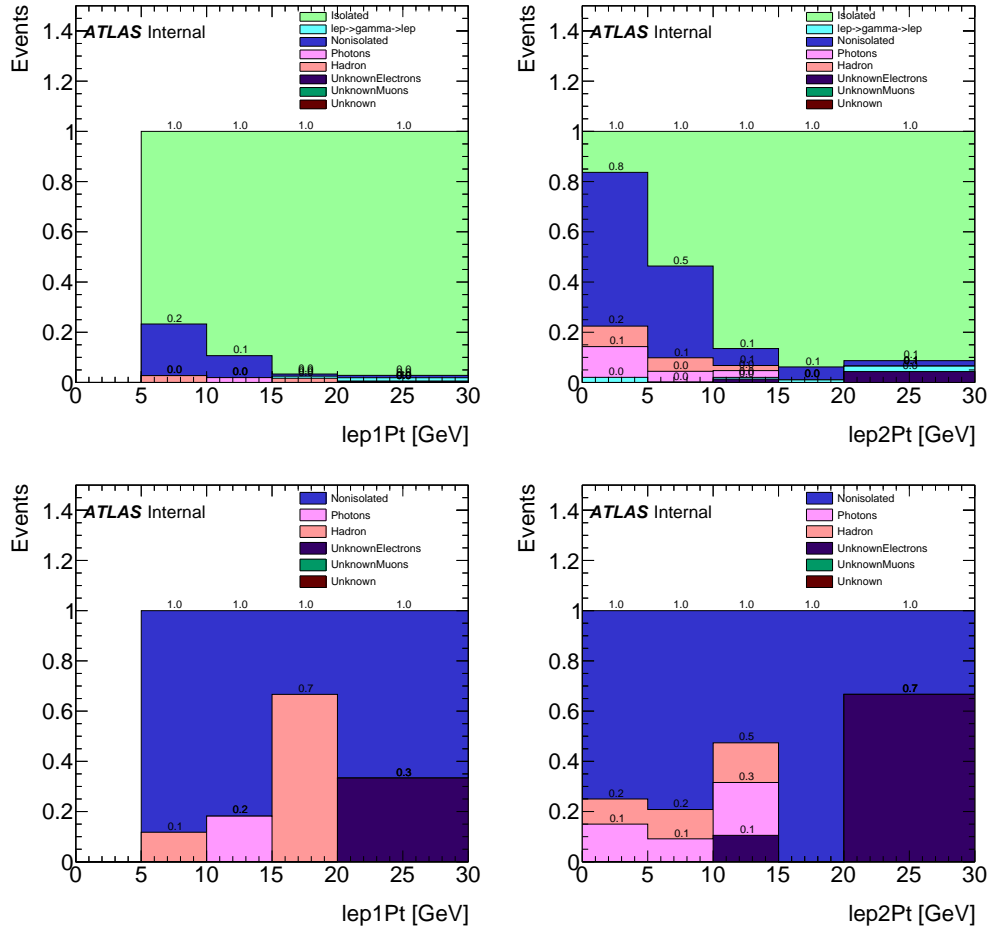


Figure 6.7: Fake lepton composition as a function of leading and subleading lepton  $p_T$ , with and without prompt (“Isolated” plus “ $\text{lep} \rightarrow \text{gamma} \rightarrow \text{lep}$ ”) leptons, for same sign electron pairs in the signal region.

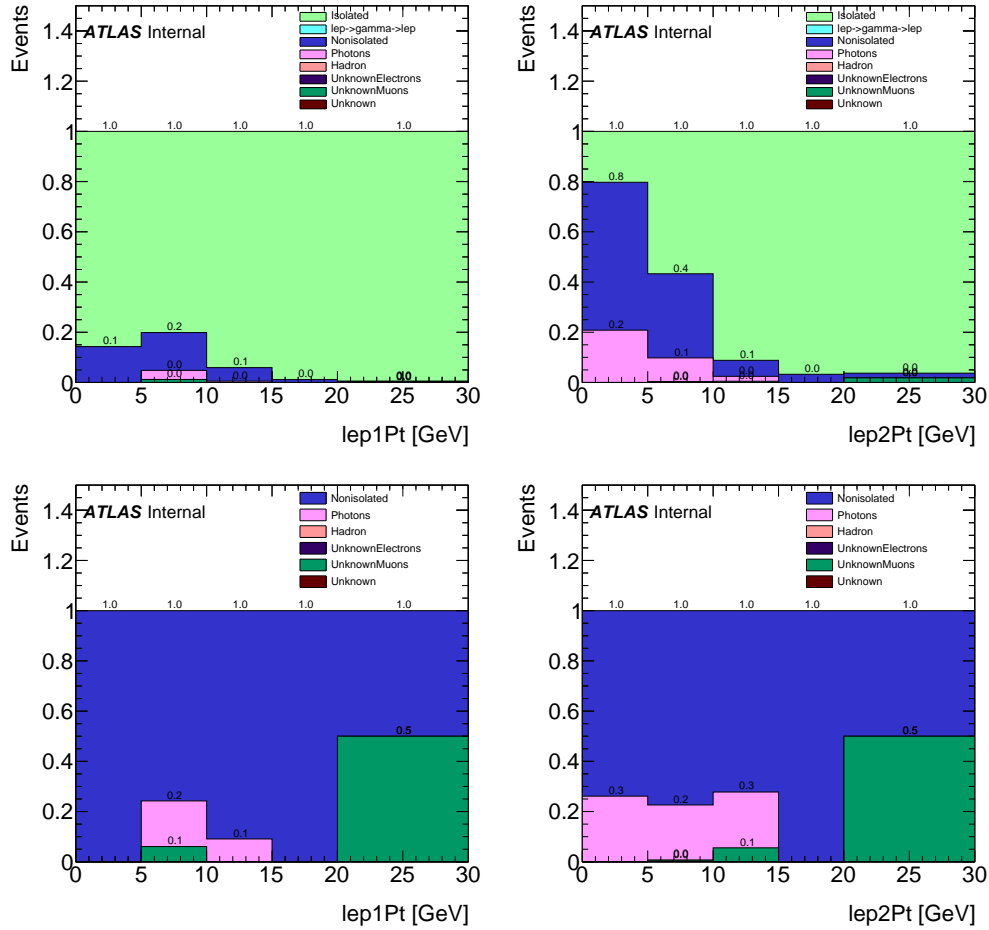


Figure 6.8: Fake lepton composition as a function of leading and subleading lepton  $p_T$ , with and without prompt (“Isolated” plus “ $\text{lep} \rightarrow \text{gamma} \rightarrow \text{lep}$ ”) leptons, for same sign muon pairs in the signal region.

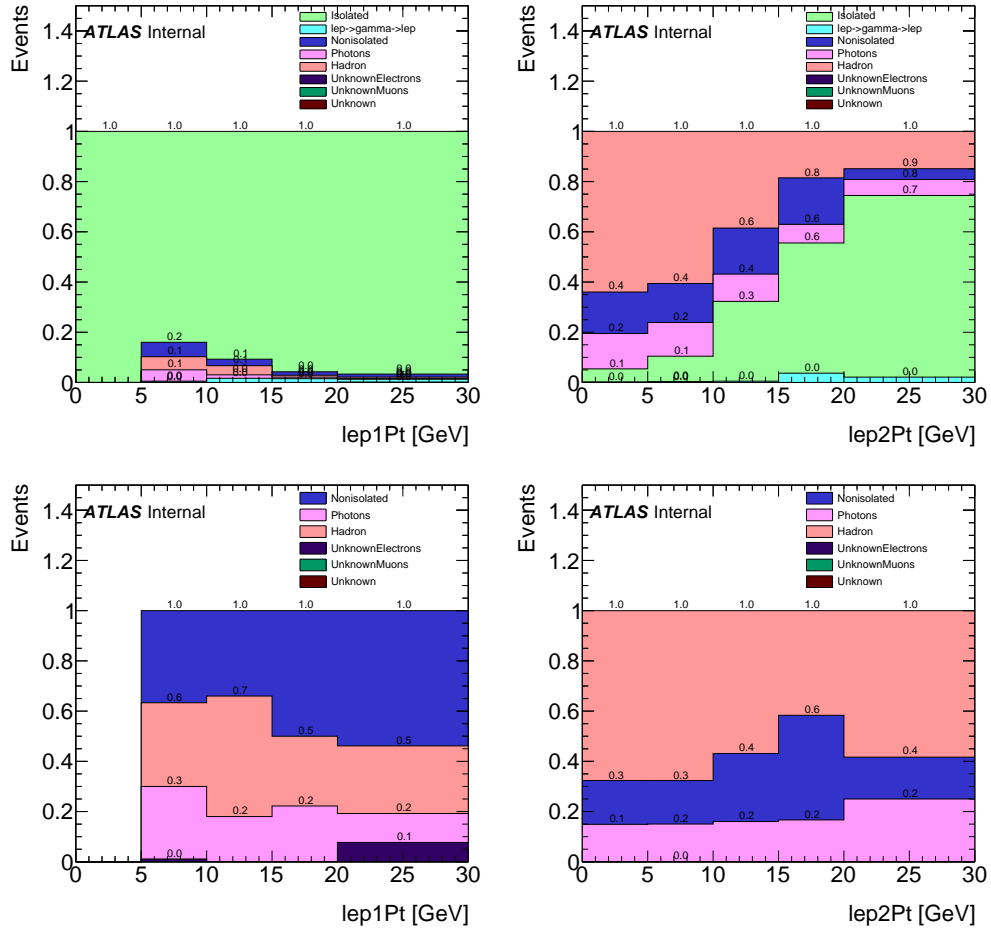


Figure 6.9: Fake lepton composition as a function of leading and subleading lepton  $p_T$ , with and without prompt (“Isolated” plus “lep $\rightarrow$ gamma $\rightarrow$ lep”) leptons, for same sign electron pairs in the fake lepton control region.

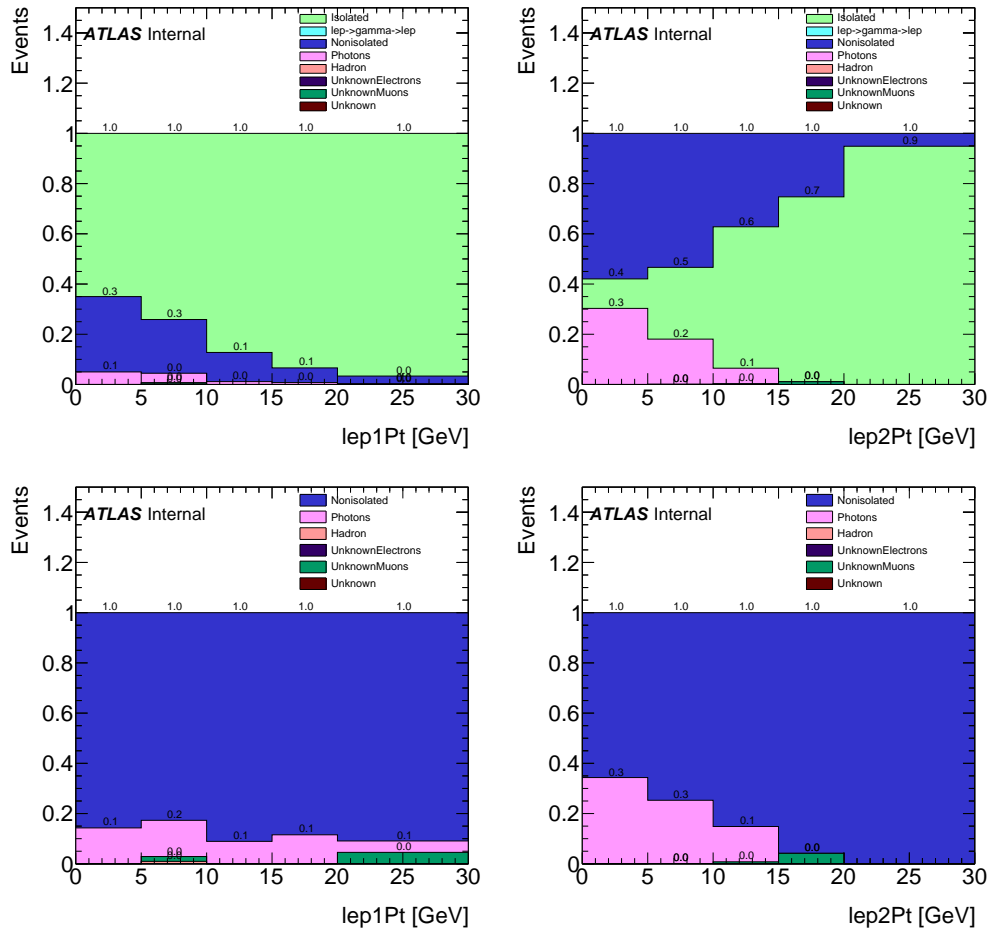


Figure 6.10: Fake lepton composition as a function of leading and subleading lepton  $p_T$ , with and without prompt (“Isolated” plus “le $\rightarrow$ γ $\rightarrow$ le”) leptons, for same sign muon pairs in the fake lepton control region.

### 6.3.2 Anti-identified Lepton Definitions

- Anti-ID definition chosen to enhance fake and non-prompt leptons while suppressing real prompt leptons.
- Enhancement is obtained by easing or inverting identification cuts used to suppress lepton misidentification
- Tighter anti-ID cuts reduces systematic uncertainties on the fake background prediction.
- Tighter anti-ID cuts increases the statistical uncertainty on the fake background prediction.

#### 6.3.2.1 Anti-ID Electrons

Signal Electron Definition
$p_T > 4.5 \text{ GeV}$
$ \eta  < 2.47$
$ z_0 \sin \theta  < 0.5 \text{ mm},  d_0/\sigma(d_0)  < 5$
Pass <i>Tight Identification</i>
Pass <i>GradientLoose Isolation</i>
Electron <i>author ! = 16</i>

Table 6.2: Summary of signal electron definitions.

Electrons
$p_T > 4.5 \text{ GeV}$
$ \eta  < 2.47$
$ z_0 \sin \theta  < 0.5 \text{ mm}$
Pass <i>LooseAndBLayer</i> Identification
NOT <i>Tight</i> Identification or $ d_0/\sigma(d_0)  > 5$ or NOT <i>GradientLoose</i> Isolation

Table 6.3: Summary of anti-ID electron definitions.

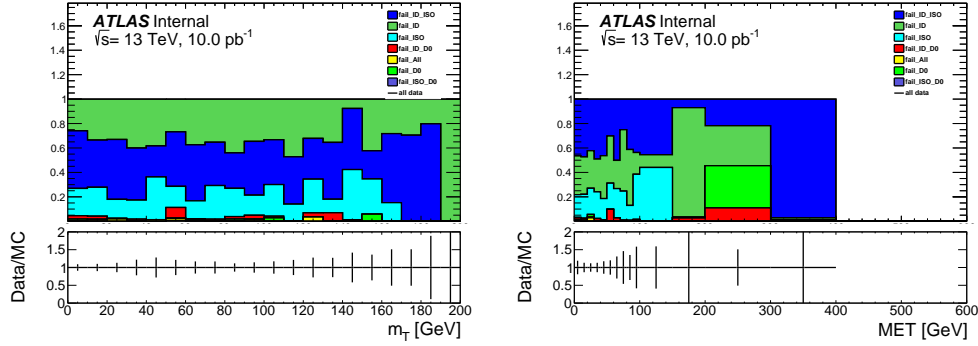


Figure 6.11: Fake electron composition as a function of  $m_T$  for events in the full  $m_T$  range (left) and as a function of  $E_T^{\text{miss}}$  (top) for events in the range  $m_T < 40 \text{ GeV}$ .

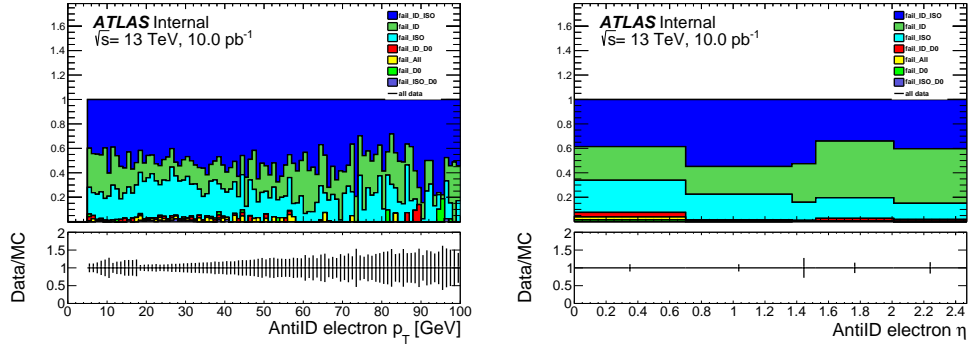


Figure 6.12: Fake electron composition as a function of denominator electron  $p_T$  (left) and as a function of denominator electron  $\eta$  (top) for events with  $m_T < 40 \text{ GeV}$ .

### 6.3.2.2 Anti-ID Muons

Signal Muon Definition
$p_T > 4 \text{ GeV}$
$ \eta  < 2.5$
$ z_0 \sin \theta  < 0.5 \text{ mm},  d_0/\sigma(d_0)  < 3$
Pass <i>Medium Identification</i>
Pass <i>FixedCutTightTrackOnly Isolation</i>

Table 6.4: Summary of signal muon definitions.

Anti-ID Muon Definition
$p_T > 4 \text{ GeV}$
$ \eta  < 2.5$
$ z_0 \sin \theta  < 0.5 \text{ mm}$
Pass <i>Medium Identification</i>
$ d_0/\sigma(d_0)  > 3 \text{ or NOT } FixedCutTightTrackOnly \text{ Isolation}$

Table 6.5: Summary of anti-ID muon definitions.

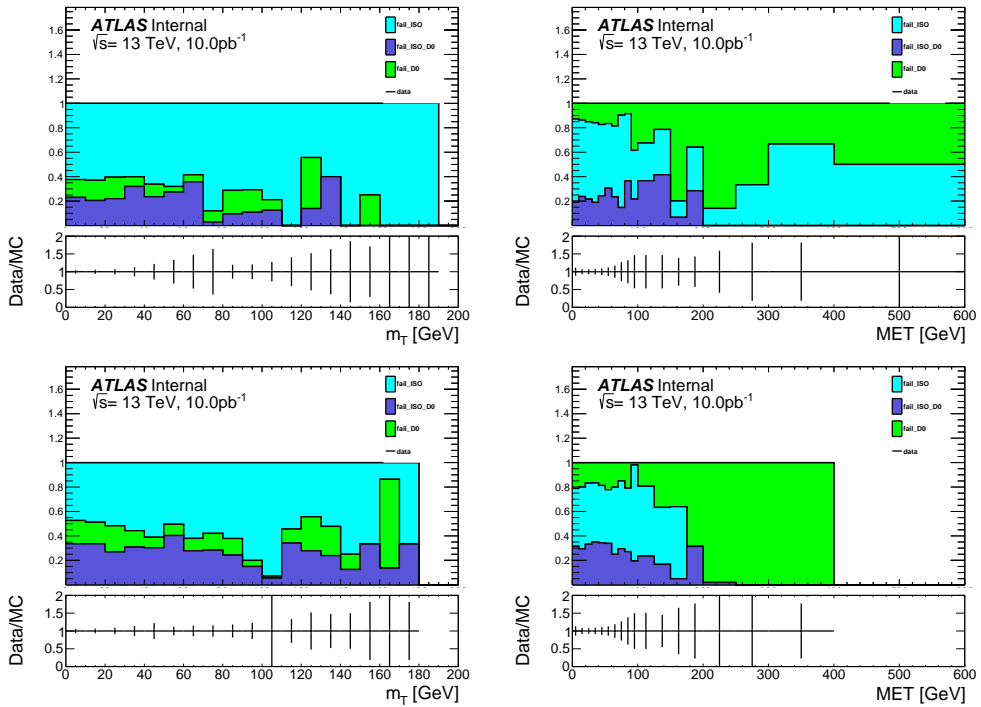


Figure 6.13: Anti-ID muon composition in events with exactly zero  $b$ -jets (top) and one or more  $b$ -jets (bottom) as a function of  $m_T$  (left) and as a function of  $E_T^{\text{miss}}$  (right). The  $E_T^{\text{miss}}$  distribution corresponds to events with  $m_T < 40 \text{ GeV}$ .

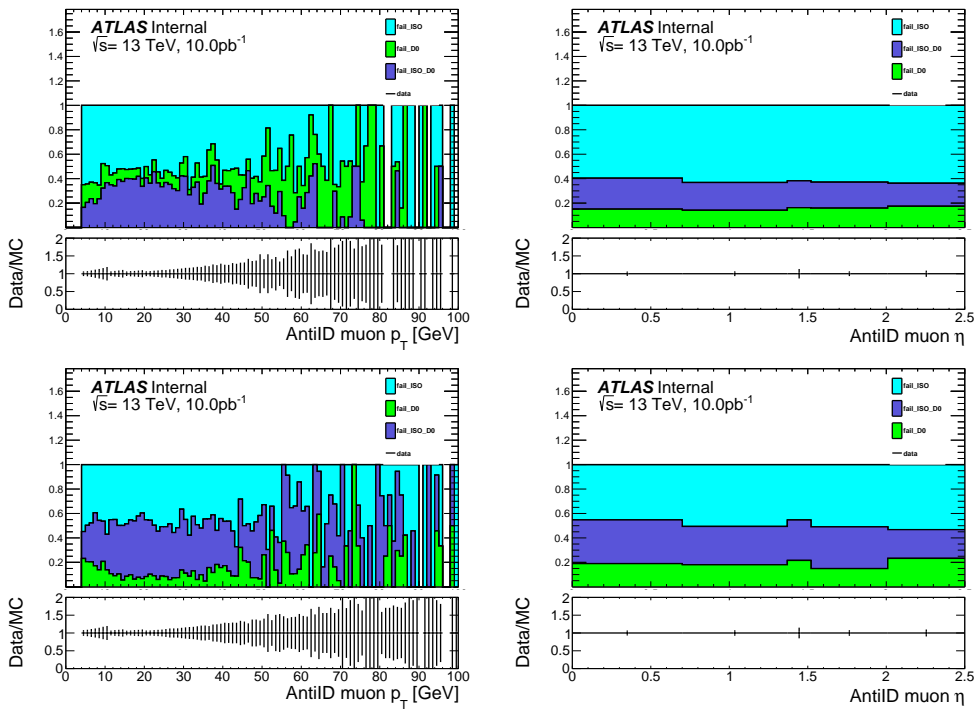


Figure 6.14: Anti-ID muon composition in events with exactly zero  $b$ -jets (top) and one or more  $b$ -jets (bottom) as a function of denominator muon  $p_T$  (left) and as a function of denominator muon  $\eta$  (right) for events with  $m_T < 40$  GeV.

### 6.3.3 Fake Factor Measurement

Electron fake factors show the largest dependance on electron  $p_T$ , but also display a dependence on the leading jet  $p_T$ , which is evident in Fig. 6.18 that shows electron fake factors as a function of electron  $p_T$  and leading jet  $p_T$  separately. Given this trend, and the fact that all signal regions used in this analysis require a hard jet with  $p_T$  greater than 100 GeV, we design the fake factor measurement region to also require a hard jet of  $p_T$  greater than 100 GeV. Fake factors as a function of other kinematic variables are also studied as a cross-check and for understanding systematic uncertainties.

Final fake factors computed as a function of electron  $p_T$  are shown in Fig. 6.19a. In addition, fake factors as functions of other variables are also inspected to check for significant trends:

- the dependence of the fake factors on  $|\eta|$  is shown in Fig. 6.19b,
- fake factors as a function of leading jet  $p_T$  and  $\Delta\phi_{jet-E_T^{\text{miss}}}$  are shown in Fig. 6.20,
- fake factors as a function of jet multiplicity and  $b$ -jet multiplicity are shown in Fig. 6.21,

el trigger	$p_T$ range [GeV]
HLT_e5_lvloose	5–11
HLT_e10_lvloose_L1EM7	11–18
HLT_e15_lvloose_L1EM13VH	18–23
HLT_e20_lvloose	> 23

Table 6.6: Single-Electron triggers used for fake factor computation and their corresponding  $p_T$  range.

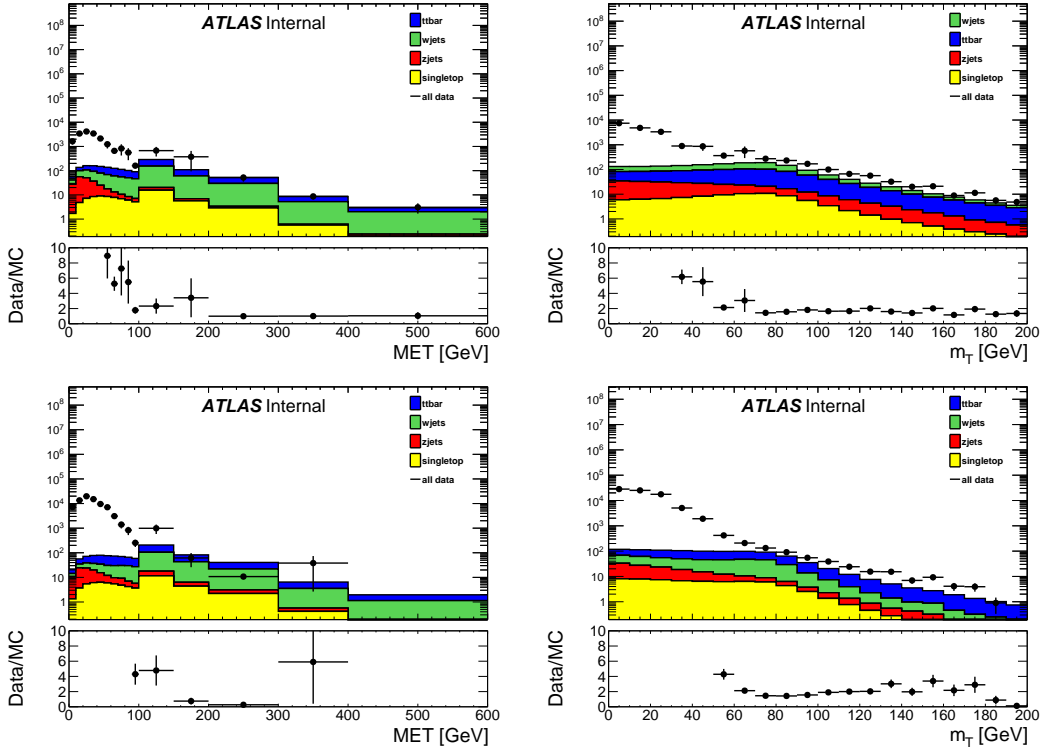


Figure 6.15: The  $E_T^{\text{miss}}$  (left) and  $m_T$  (right) distributions for numerator (top) and denominator (bottom) electrons in the pre-scaled single-lepton-trigger sample. MC has been scaled to the data in the  $E_T^{\text{miss}} > 200$  GeV region.

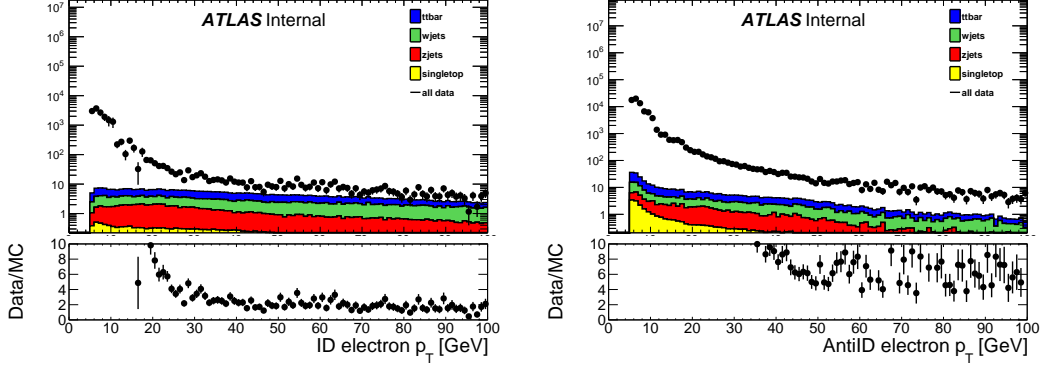


Figure 6.16: Electron  $p_T$  for numerator (left) and denominator (right) objects in the pre-scaled single-lepton-trigger sample for events with  $m_T < 40$  GeV. MC has been scaled to the data in the  $E_T^{\text{miss}} > 200$  GeV region.

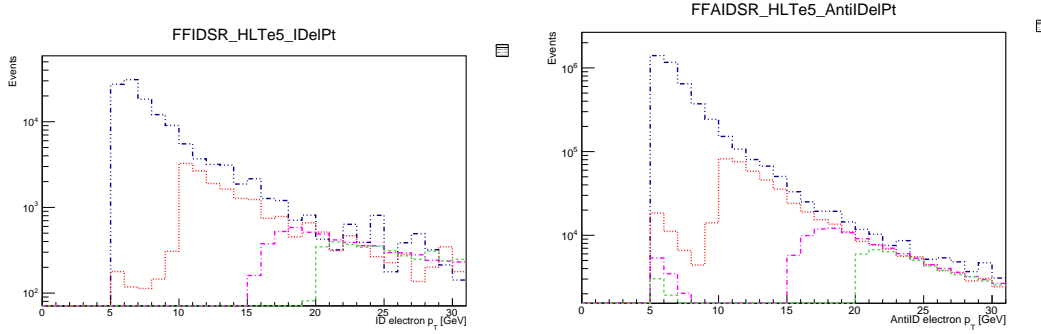


Figure 6.17: The numerator electron (left) and denominator electron (right)  $p_T$  distributions for pre-scaled single-lepton-trigger, normalized to  $1 \text{ pb}^{-1}$ . Blue curve: HLT\_e5\_lvhloose, red curve: HLT\_e10\_lvhloose\_L1EM7, purple curve: HLT\_e15\_lvhloose\_L1EM13, green curve: HLT\_e20\_lvhloose.

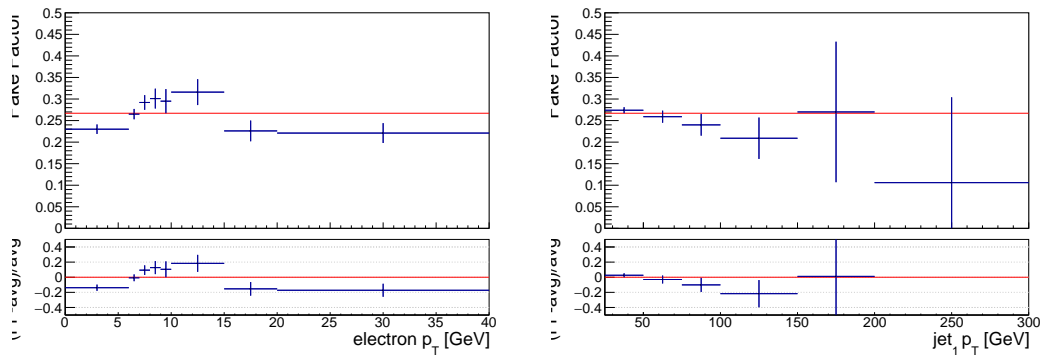


Figure 6.18: Electron fake factors *before* requiring a hard jet of  $p_T > 100 \text{ GeV}$ , computed from single-electron prescaled triggers as a function of electron  $p_T$  (left) and leading jet  $p_T$  (right). Fake factors for electron  $p_T 4.5 - 5 \text{ GeV}$  are taken to be the same as electron  $p_T 5 - 6 \text{ GeV}$ . A red line denotes the average electron fake factor over all electron  $p_T$  of 0.267.

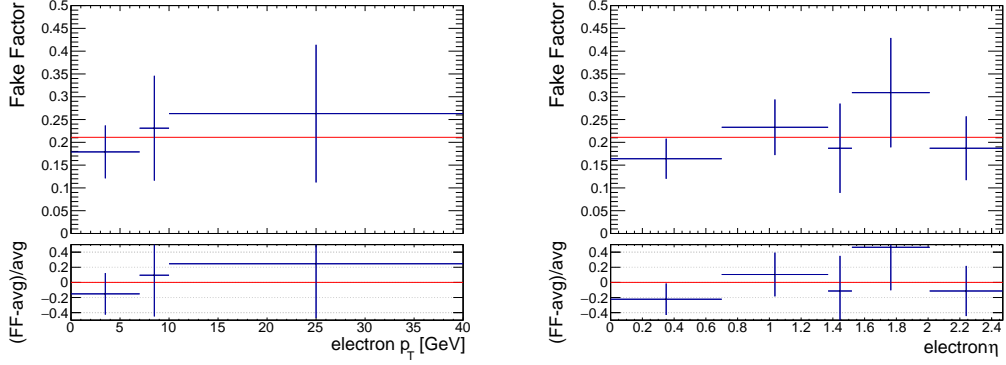


Figure 6.19: Electron fake factors computed from single-electron prescaled triggers as a function of electron  $p_T$  (left) and electron  $\eta$  (right) in the kinematic region with leading  $\text{jet}p_T > 100\text{GeV}$ . Fake factors for electron  $p_T$  4.5 – 5 GeV are taken to be the same as electron  $p_T$  5 – 6 GeV. A red line denotes the average electron fake factor over all electron  $p_T$  of 0.211.

- fake factors as a function of pile up variables, such as average interaction per bunch crossing and number of primary vertices, are also shown in Fig. 6.22.

The relative uncertainties on the final electron fake factors versus electron  $p_T$  are shown in Fig. 6.23.

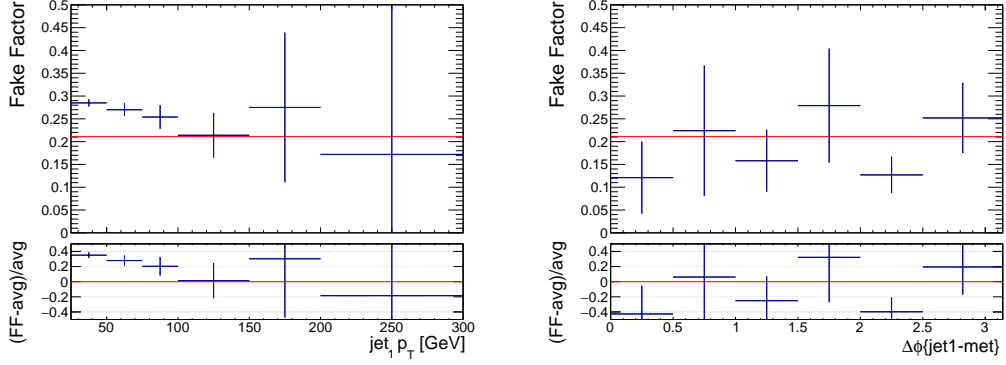


Figure 6.20: Electron fake factors computed from single-electron prescaled triggers as a function of leading jet  $p_T$  (left) and  $\Delta\phi_{jet-E_T^{\text{miss}}}$  (right). A red line denotes the average electron fake factor over all electron  $p_T$  of 0.211.

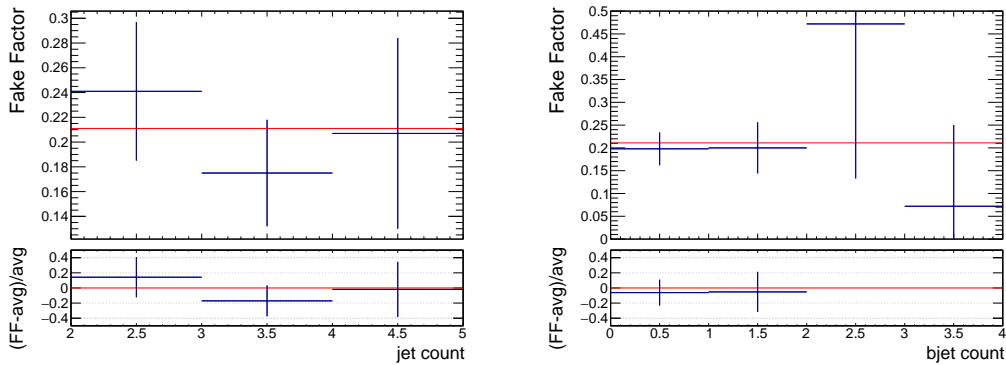


Figure 6.21: Electron fake factors computed from single-electron prescaled triggers as a function of the jet multiplicity (left) and the  $b$ -jet multiplicity (right). A red line denotes the average electron fake factor over all electron  $p_T$  of 0.211.

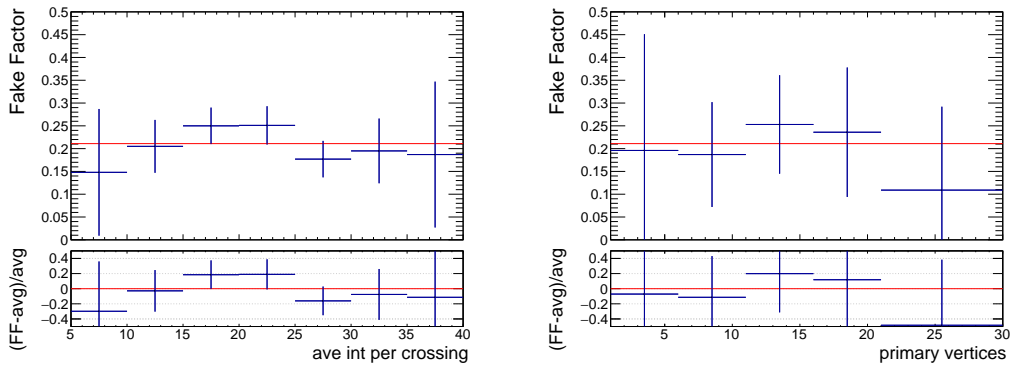


Figure 6.22: Electron fake factors computed from single-electron prescaled triggers as a function of the average interaction per bunch crossing (left) and the number of primary vertices (right). A red line denotes the average electron fake factor over all electron  $p_T$  of 0.211.

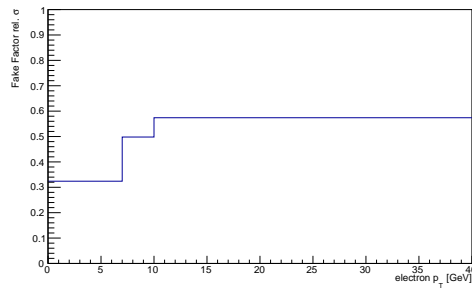


Figure 6.23: Relative uncertainties on electron fake factors binned electron  $p_T$ .

The muon fake factors are derived in a very similar way as the electron fake factors. The “numerator” muons, also called th ID muons, are the same as signal muons as defined in Section ??, which are baseline muons that are required to pass `FixedCutTightTrackOnly` isolation and  $|d_0/\sigma(d_0)| < 3.0$ . ”Denominator” muons, also called anti-ID muons, are defined as baseline muons that fail at least one of the signal muon requirements, i.e. they are required to fail either the `FixedCutTightTrackOnly` isolation or  $|d_0/\sigma(d_0)| < 3.0$ . All numerators and denominators are required to pass the  $|z_0 \sin \theta| < 0.5$  mm requirement to reduce the impact of pileup. One notable difference with respect to the signal muon requirements is that the muon-jet overlap removal is relaxed when performing the fake factor measurement<sup>1</sup>.

The decomposition of denominator muons in all events according to which ID criteria or combination of ID criteria failed is shown in Fig 6.5 and Fig 6.6. The  $m_T$  distribution of this decomposition in Fig 6.5 is plotted over the entire  $m_T$  range, while the  $E_T^{\text{miss}}$  distribution in Fig 6.5 and the  $p_T$  and  $\eta$  distributions in Fig 6.6 are all shown for  $m_T < 40$  GeV. Note that these distributions are separated into categories: one for events with exactly zero  $b$ -jets, and another for events with one or more  $b$ -jets.

Both data and MC contributions to the numerator and denominator samples in the single-muon trigger sample are normalized to  $10 \text{ pb}^{-1}$ , to remove the effects of the prescales in the data. The MC is then re-scaled to the data in events with  $E_T^{\text{miss}} > 200$  GeV, a kinematic region expected to pure in prompt leptons. For events

---

<sup>1</sup>This enhances the statistics used for deriving the fake factors, and is motivated by the observation that the muon-jet overlap removal is primarily designed to reduce the number of heavy flavor decays which are inadvertently being classified as signal muons, i.e. a sample of events that is interesting to keep for a fake measurement.

with exactly 0  $b$ -jets, the MC re-scaling factor for numerator muons is  $1.01 \pm 0.13$ , for denominator muons it is  $1.20 \pm 0.29$ . For events with one or more  $b$ -jets, the MC re-scaling factor for numerator muons is  $1.24 \pm 0.20$ , for denominator muons it is  $7.34 \pm 5.00$ . If instead, the MC is re-scaled to match the data for events with  $m_T > 100$  GeV, a region that should also be pure in prompt leptons, the re-scaling factors for events with exactly 0  $b$ -jets are  $2.37 \pm 0.10$  for numerator muons and  $11.68 \pm 2.28$  for denominator muons; events with one or more  $b$ -jets have re-scale factors  $1.60 \pm 0.06$  for numerator muons and  $10.41 \pm 6.34$  for denominator muons. The re-scaling factors vary significantly between the two methods but the fake factors themselves exhibit small changes between the two methods and can be used as a systematic uncertainty.

Distributions of  $E_T^{\text{miss}}$  and  $m_T$  for numerator and denominator muons for events with exactly zero  $b$ -jets are shown in Fig. 6.24, and for events with one or more  $b$ -jets in Fig. 6.25. Muon  $p_T$  distributions for events with exactly zero  $b$ -jet are shown in Fig. 6.26, and for events with one or more  $b$ -jets in Fig. 6.27.

The fake factors are computed using events with  $m_T < 40$  GeV, using the distribution in Figs. 6.26 and 6.27, as

$$F(p_T) = \frac{\text{Numerator}_{\text{data}} - \text{Numerator}_{\text{MC}}}{\text{Denominator}_{\text{data}} - \text{Denominator}_{\text{MC}}} \quad (6.2)$$

where the fake factor  $F$  is computed in discrete  $p_T$  bins with different single-muon triggers applied. The specific trigger applied to each range in lepton  $p_T$  was chosen to reduce the effect of the trigger turn on and maintain good statistics. Muon  $p_T$  distributions for the prescaled triggers shown in Fig. 6.28 are arbitrarily normalized to

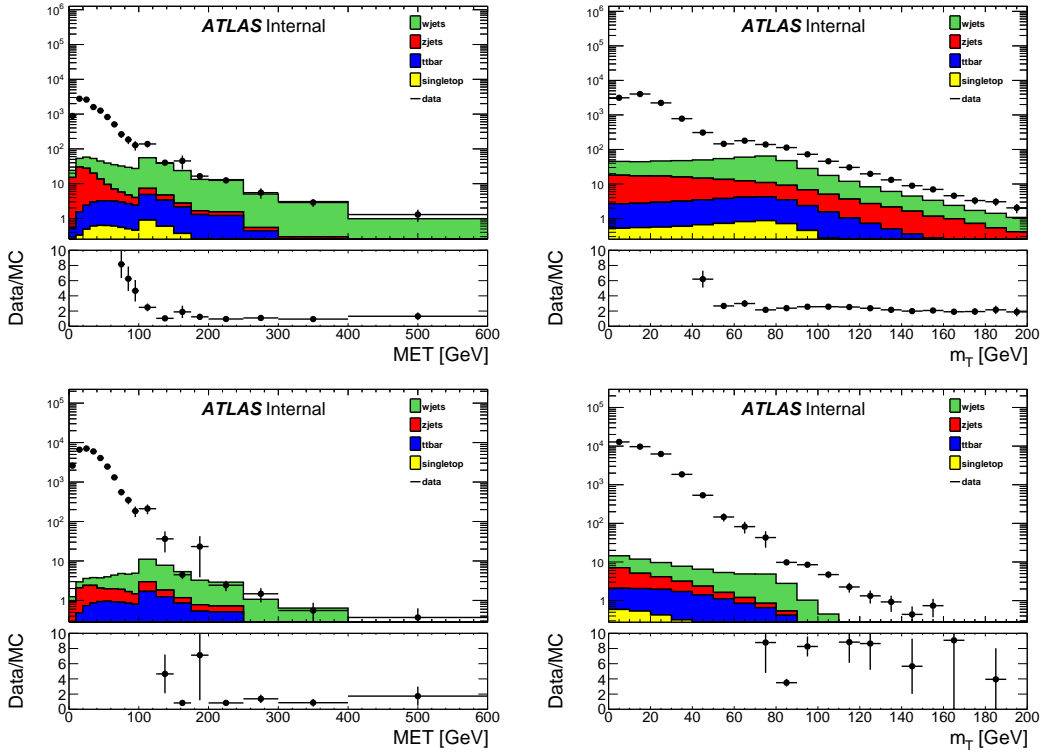


Figure 6.24: The  $E_T^{\text{miss}}$  (left) and  $m_T$  (right) distributions for numerator (top) and denominator (bottom) muons in the prescaled single-lepton-trigger sample for events with exactly zero  $b$ -jets. MC has been scaled to the data in the  $E_T^{\text{miss}} > 200$  GeV region.

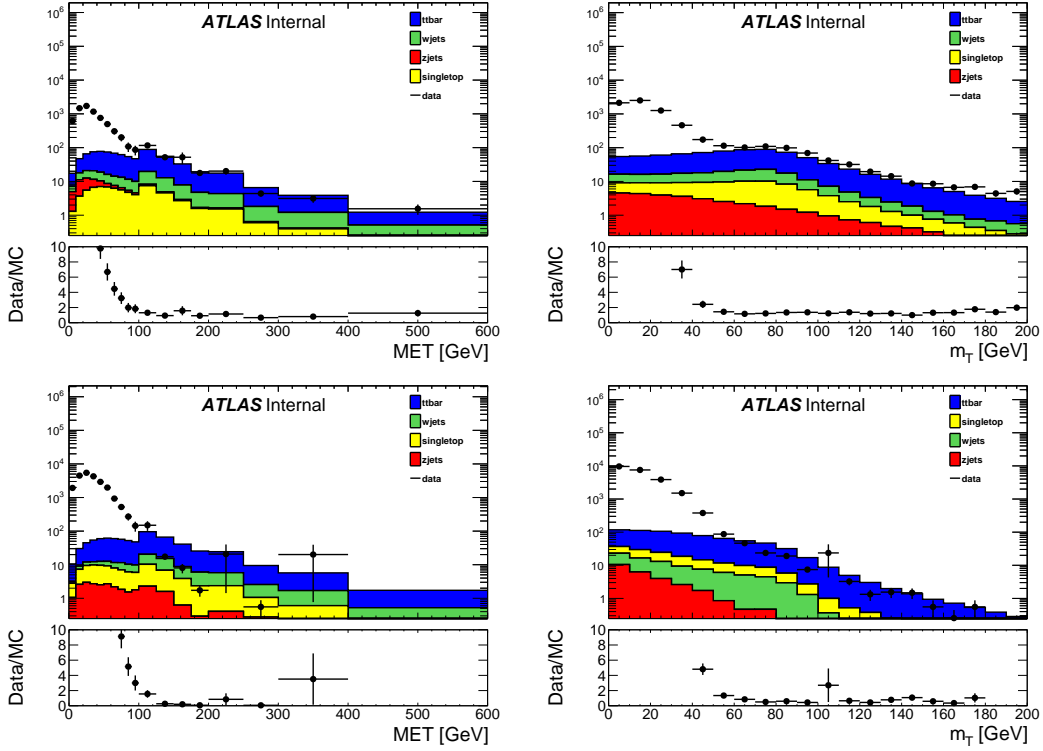


Figure 6.25: The  $E_T^{\text{miss}}$  (left) and  $m_T$  (right) distributions for numerator (top) and denominator (bottom) muons in the prescaled single-lepton-trigger sample for events with one or more  $b$ -jets. MC has been scaled to the data in the  $E_T^{\text{miss}} > 200$  GeV region.

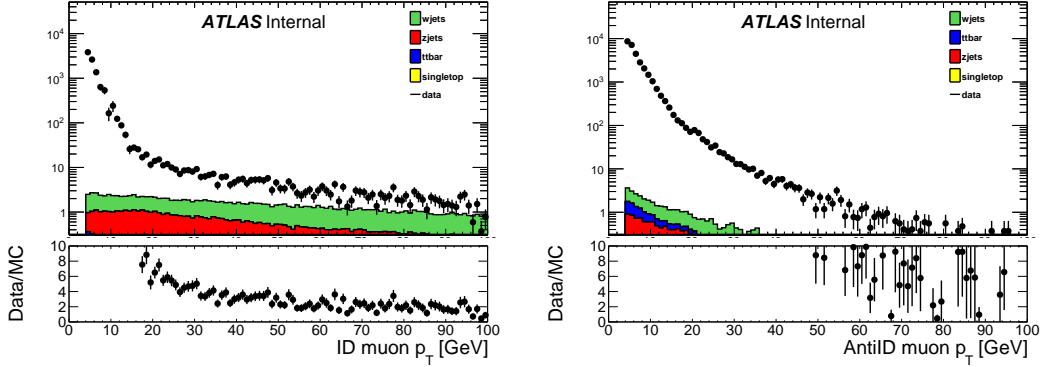


Figure 6.26: Muon  $p_T$  for numerator (left) and denominator (right) objects in the prescaled single-muon trigger sample for events with  $m_T < 40$  GeV. MC has been scaled to the data in the  $m_T > 100$  GeV region. Distributions from [?].

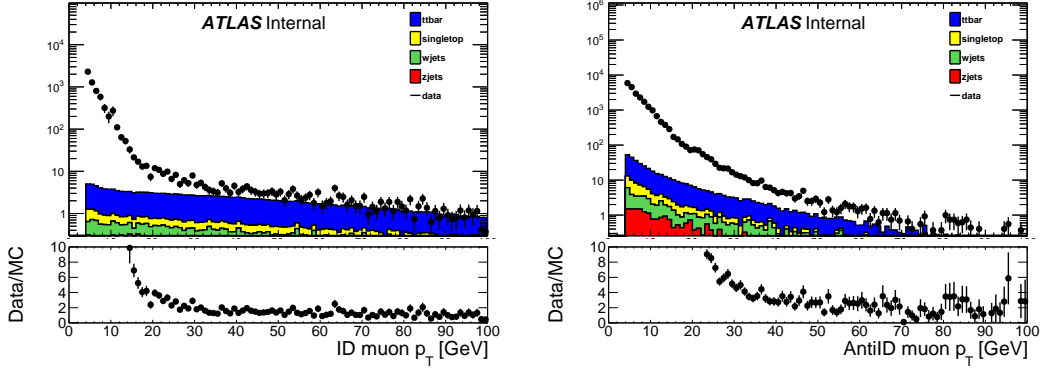


Figure 6.27: Muon  $p_T$  for numerator (left) and denominator (right) objects in the prescaled single-muon trigger sample for events with  $m_T < 40$  GeV. MC has been scaled to the data in the  $m_T > 100$  GeV region. Distributions from [?].

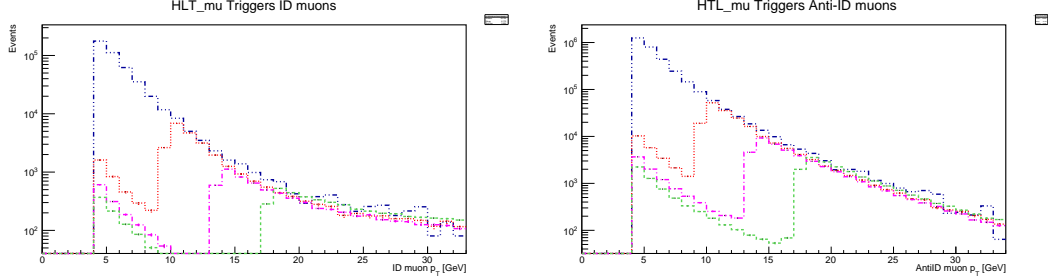


Figure 6.28: The numerator muon (left) and denominator denominator (right)  $p_T$  distributions for prescaled single-muon triggers, normalized to  $1 \text{ pb}^{-1}$ . Blue curve: HLT\_mu4, red curve: HLT\_mu10, purple curve: HLT\_mu14, green curve: HLT\_mu18.

$1 \text{ pb}^{-1}$ . HLT\_mu4 trigger is required for muon  $p_T 4 - 11$  GeV, HLT\_mu10 is required for muon  $p_T 11 - 15$  GeV, HLT\_mu14 is required for muon  $p_T 15 - 20$  GeV, and HLT\_mu18 is required for muon  $p_T > 20$  GeV. A table of these triggers and corresponding  $p_T$  range is shown in Table 6.7

Muon fake factors depend strongly on muon  $p_T$ , but also display a systematic dependence on the leading jet  $p_T$ . Unlike the electron fake factors, there is also a separate dependence on  $b$ -jet multiplicity. Fig. 6.29 shows the muon fake factors as functions of

el trigger	$p_T$ range [GeV]
HLT_mu4	4–11
HLT_mu10	11–15
HLT_mu14	18–20
HLT_mu18	> 20

Table 6.7: Single-muon triggers used for fake factor computation and their corresponding  $p_T$  range.

muon  $p_T$ , leading jet  $p_T$ , and  $b$ -jet multiplicity before any hard jet requirement. Similar to the electron fake factor calculation, the fake factor measurement region requires a hard jet of  $p_T$  greater than 100 GeV, but unlike the electron fake factors, the muon fake factors are also separated into two  $b$ -jet multiplicity bins: exactly zero  $b$ -jets, and one or more  $b$ -jets. The bin with exactly zero  $b$ -jets is used to estimate the fake contribution in the signal region, and the bin with one or more  $b$ -jets is used to estimate the fake contribution in the  $t\bar{t}$  control region.

The final fake factors are shown in Fig. 6.30 as a functions of muon  $p_T$  for each of the  $b$ -jet multiplicity bins. In addition to the final fake factors binned in  $p_T$ , fake factors binned in other variables are also inspected to check for significant trends:

- Fake factors as a function of muon  $\eta$  are shown in Fig. 6.31,
- Fake factors as a function of  $\Delta\phi_{jet1-met}$  are shown in Fig. 6.32,
- Fake factors as a function of jet multiplicity are shown in Fig. 6.33,
- Fake factors as a function of average interactions per bunch crossing are shown in Fig. 6.34,
- Fake factors as a function of the number of primary vertices are shown in Fig. 6.35.

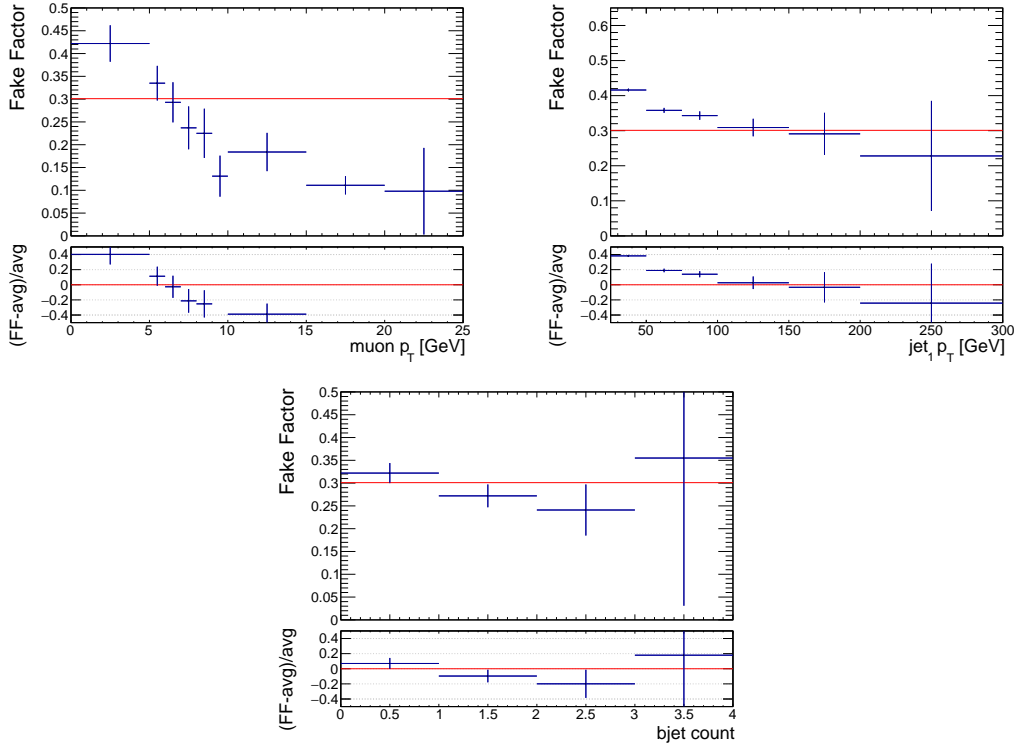


Figure 6.29: Muon fake factors *before* requiring a hard jet of  $p_T > 100$  GeV, computed from single-muon prescaled triggers as a function of muon  $p_T$  (top-left), as a function of leading jep  $p_T$  (top-right), and as a function of  $b$ -jet multiplicity (bottom). A red line denotes the average muon fake factor over all  $p_T$ .

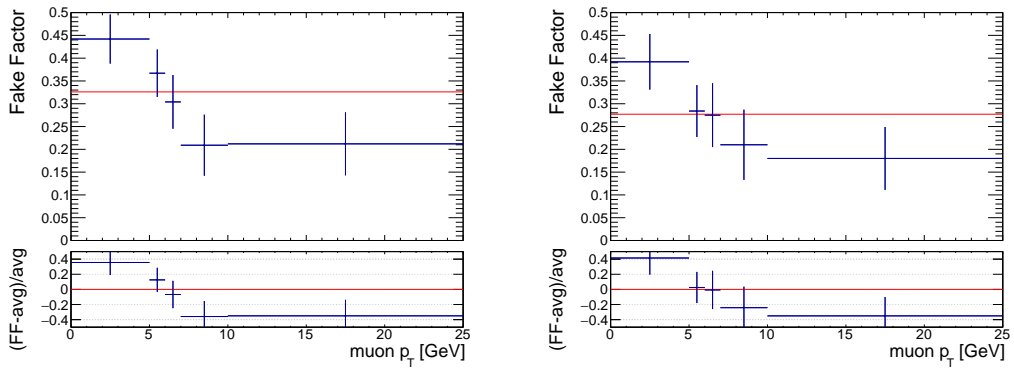


Figure 6.30: Muon fake factors computed from single-muon prescaled triggers as a function of muon  $p_T$  in events with exactly zero  $b$ -jets (left) and one or more  $b$ -jets (right). A red line denotes the average muon fake factor over all muon  $p_T$ .

The relative uncertainties on the muons fake factors versus muon  $p_T$  for the separate  $b$ -jet multiplicity bins are shown in Fig. 6.36.

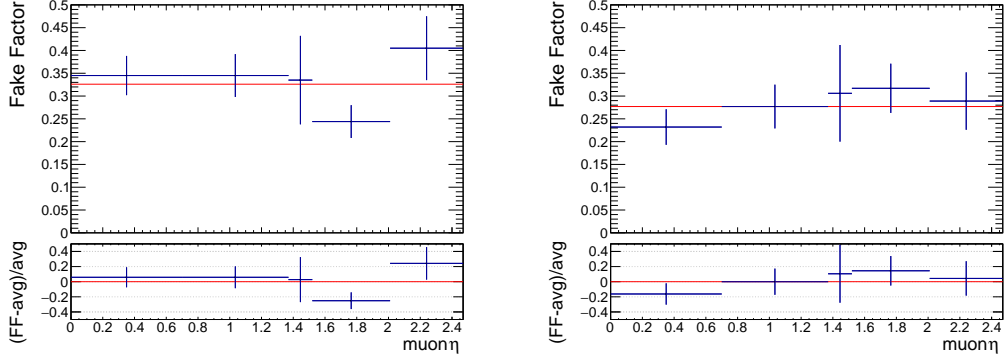


Figure 6.31: Muon fake factors computed from single-muon prescaled triggers as a function of muon  $\eta$  in events with exactly zero  $b$ -jets (left) and one or more  $b$ -jets (right). A red line denotes the average muon fake factor over all muon  $p_T$ .

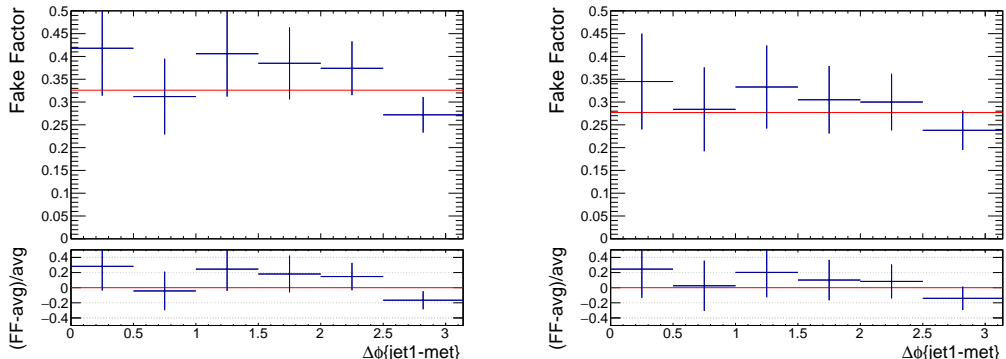


Figure 6.32: Muon fake factors computed from single-muon prescaled triggers as a function of  $\Delta\phi_{jet-E_T^{\text{miss}}}$  in events with exactly zero  $b$ -jets (left) and one or more  $b$ -jets (right). A red line denotes the average muon fake factor over all muon  $p_T$

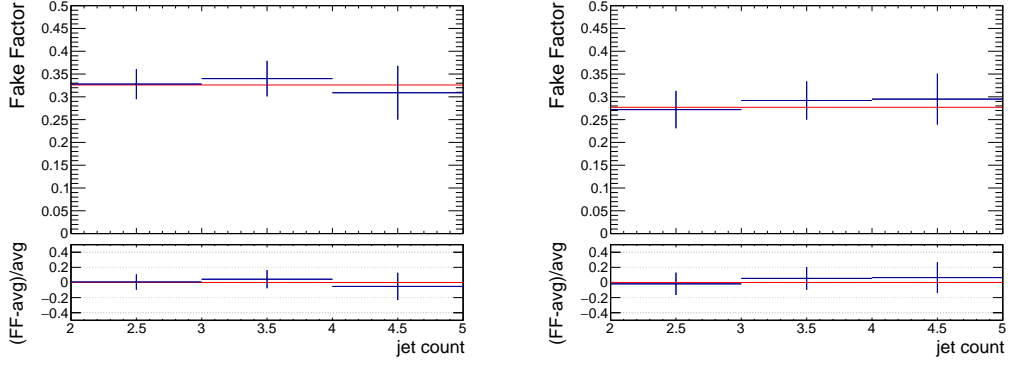


Figure 6.33: Muon fake factors computed from single-muon prescaled triggers as a function of the jet multiplicity in events with exactly zero  $b$ -jets (left) and one or more  $b$ -jets (right). A red line denotes the average muon fake factor over all muon  $p_T$

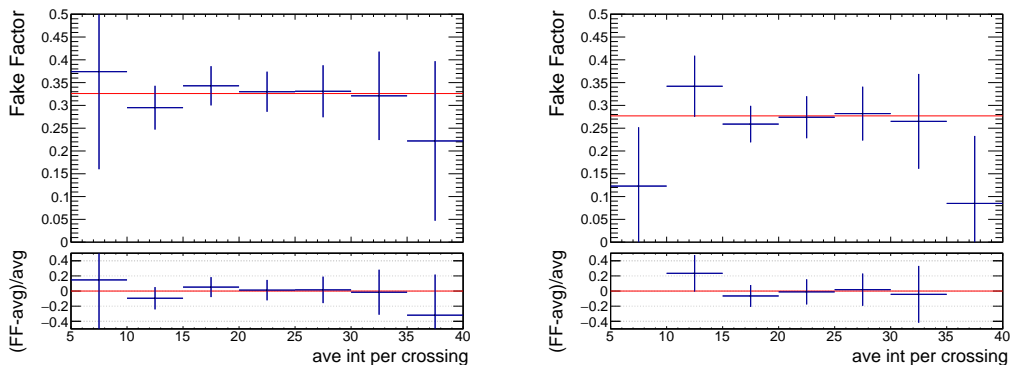


Figure 6.34: Muon fake factors computed from single-muon prescaled triggers as a function of the average number of interactions per bunch crossing in events with exactly zero  $b$ -jets (left) and one or more  $b$ -jets (right). A red line denotes the average muon fake factor over all muon  $p_T$

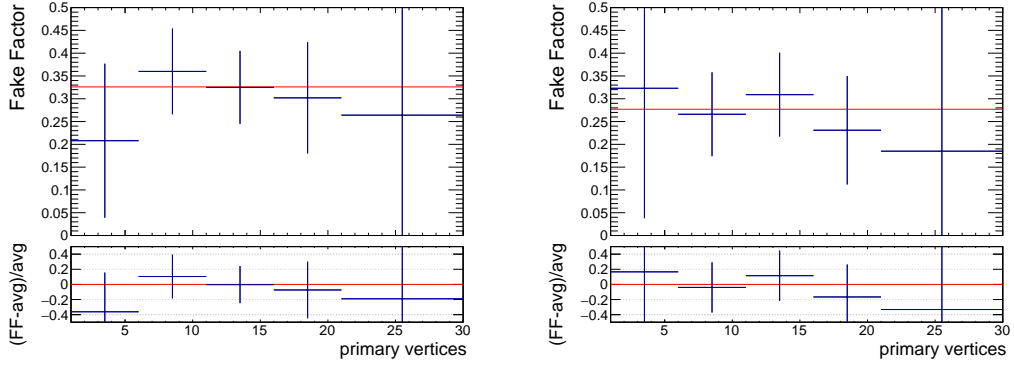


Figure 6.35: Muon fake factors computed from single-muon prescaled triggers as a function of the number of primary vertices in events with exactly zero  $b$ -jets (left) and one or more  $b$ -jets (right). A red line denotes the average muon fake factor over all muon  $p_T$

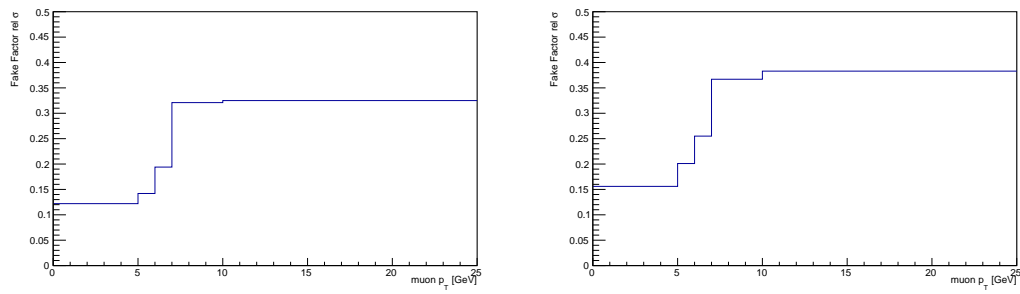


Figure 6.36: Relative uncertainties on muon fake factors versus muon  $p_T$  in zero  $b$ -jets bin (left) and one or more  $b$ -jets bin (right).

## 6.4 Conclusion

# Chapter 7

## Backgrounds

### 7.1 Fake Lepton Background

Show the calculations and results of the fake estimate. The method will be explained in a dedicated chapter/section.

### 7.2 $t\bar{t}$ Background

Mainly b-jet requirement

### 7.3 Drell-Yan Background

Off-shell  $z \rightarrow ll$  events.

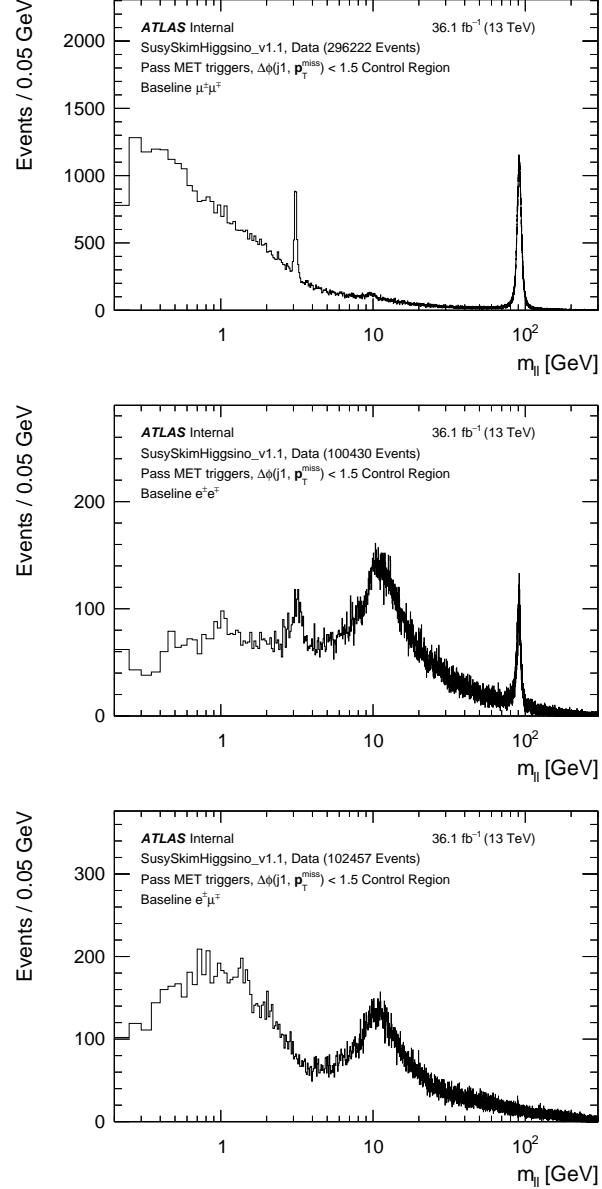


Figure 7.1: Data events passing inclusive  $E_T^{\text{miss}}$  triggers with opposite sign baseline leptons in the dilepton invariant mass  $m_{\ell\ell}$  spectrum. The  $\Delta\phi(j_1, \mathbf{p}_T^{\text{miss}})$  variable is inverted to ensure this is orthogonal to the signal region.

## 7.4 Z+jets Background

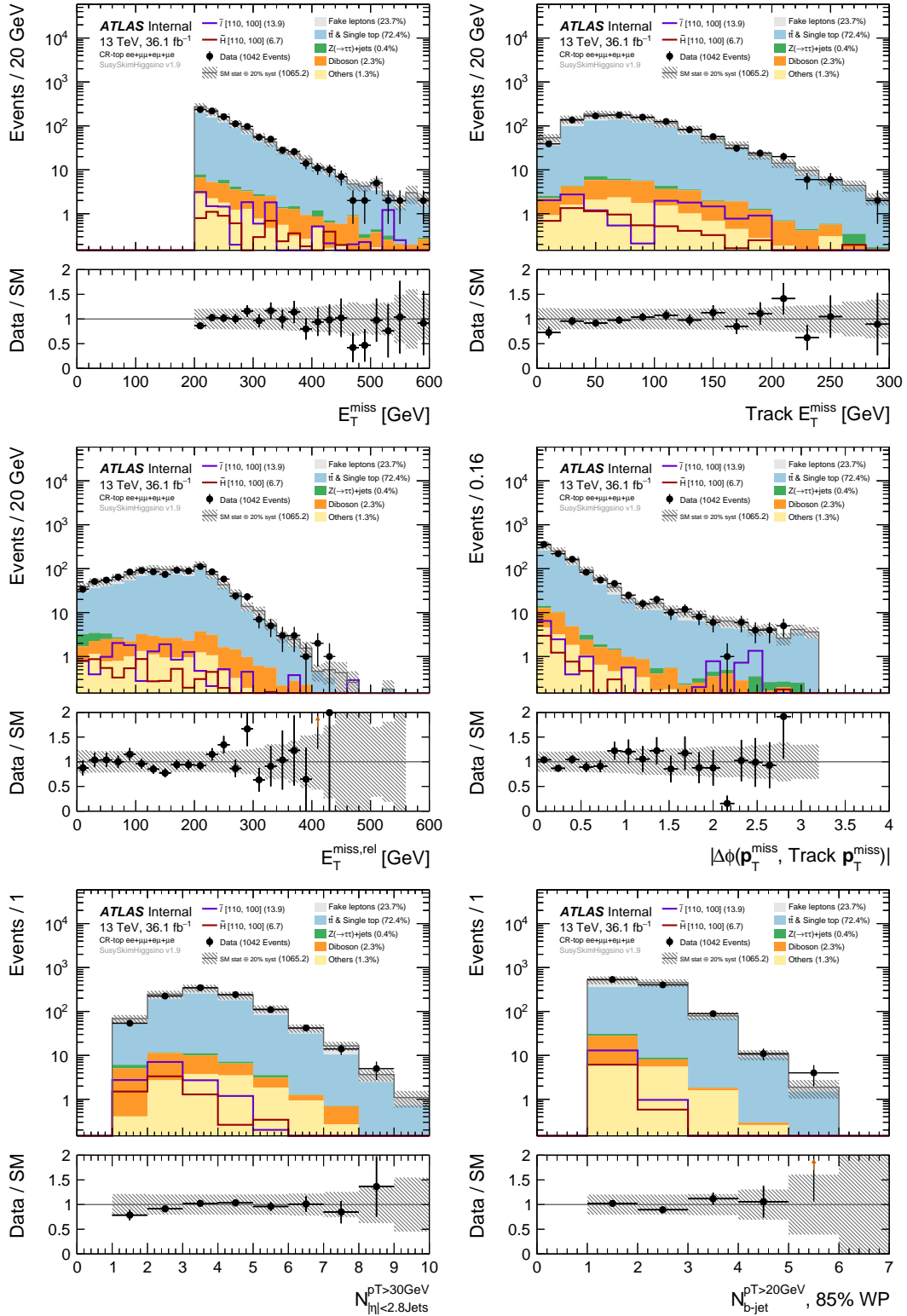


Figure 7.2: CR-top  $ee + \mu\mu + e\mu + \mu e$  channel, pre-fit distributions.  
61

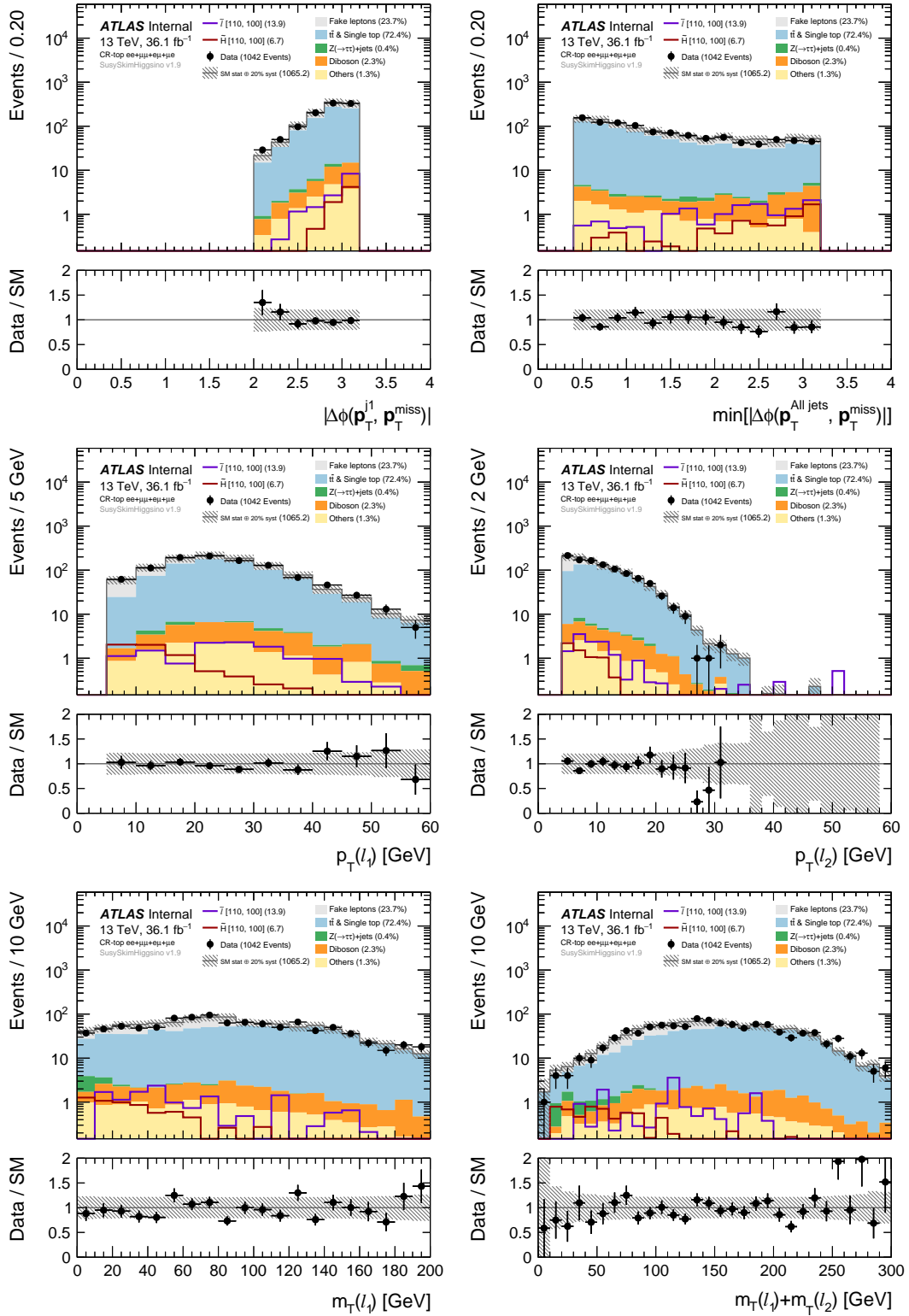


Figure 7.3:  $m_T^{\ell_1} + m_T^{\ell_2}$

Figure 7.4: CR-top  $ee + \mu\mu + e\mu + \mu e$  channel, pre-fit distributions.

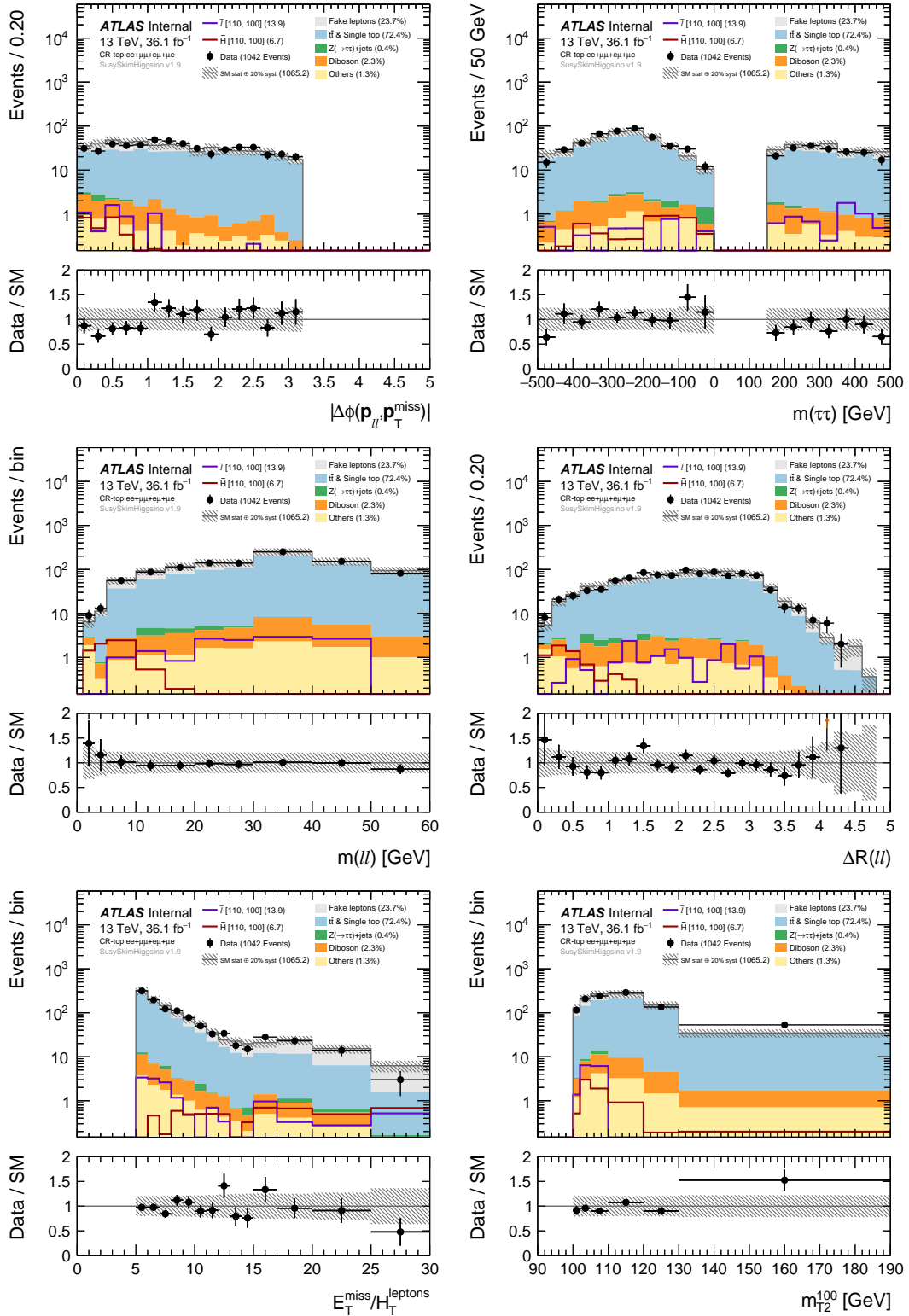
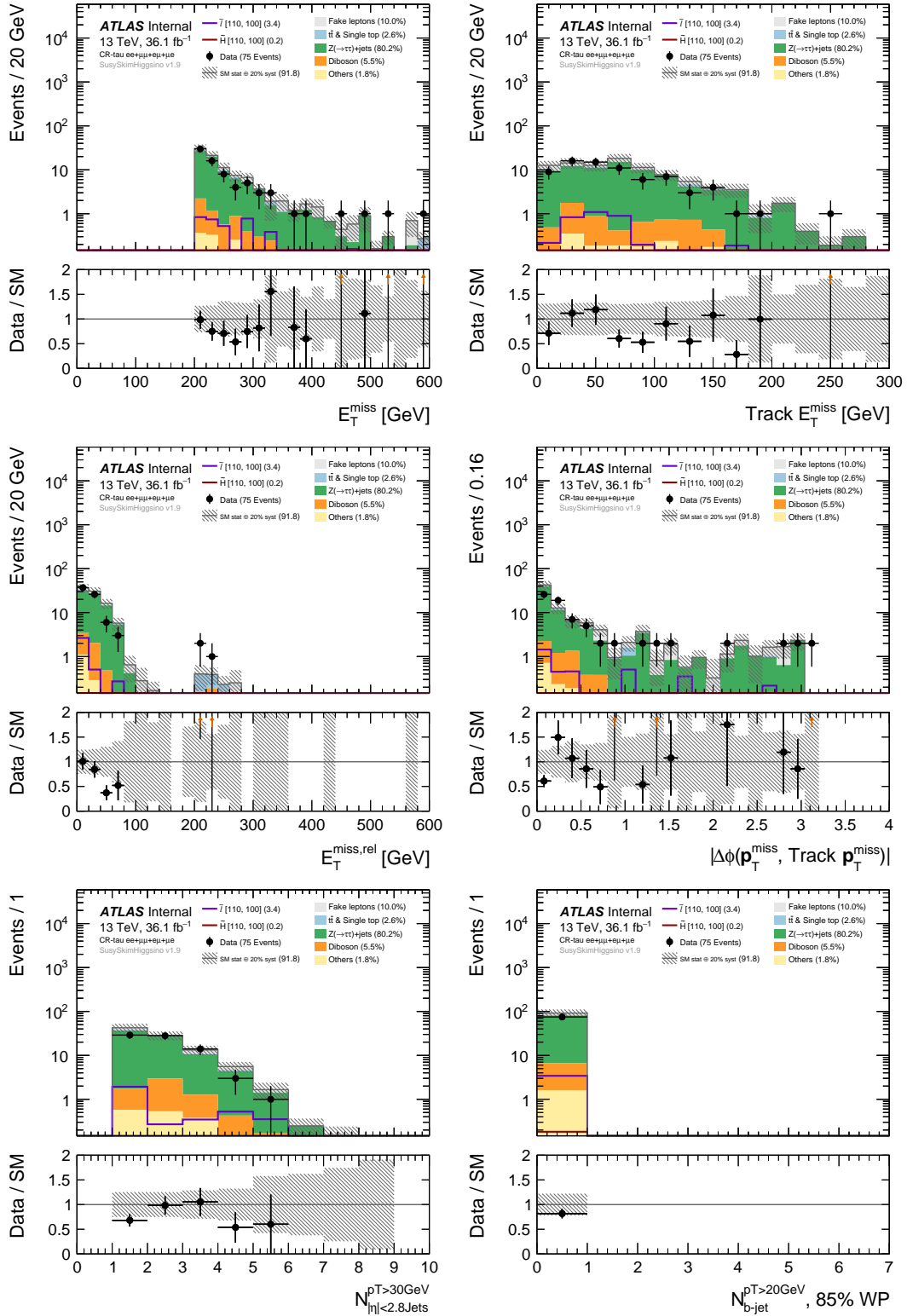
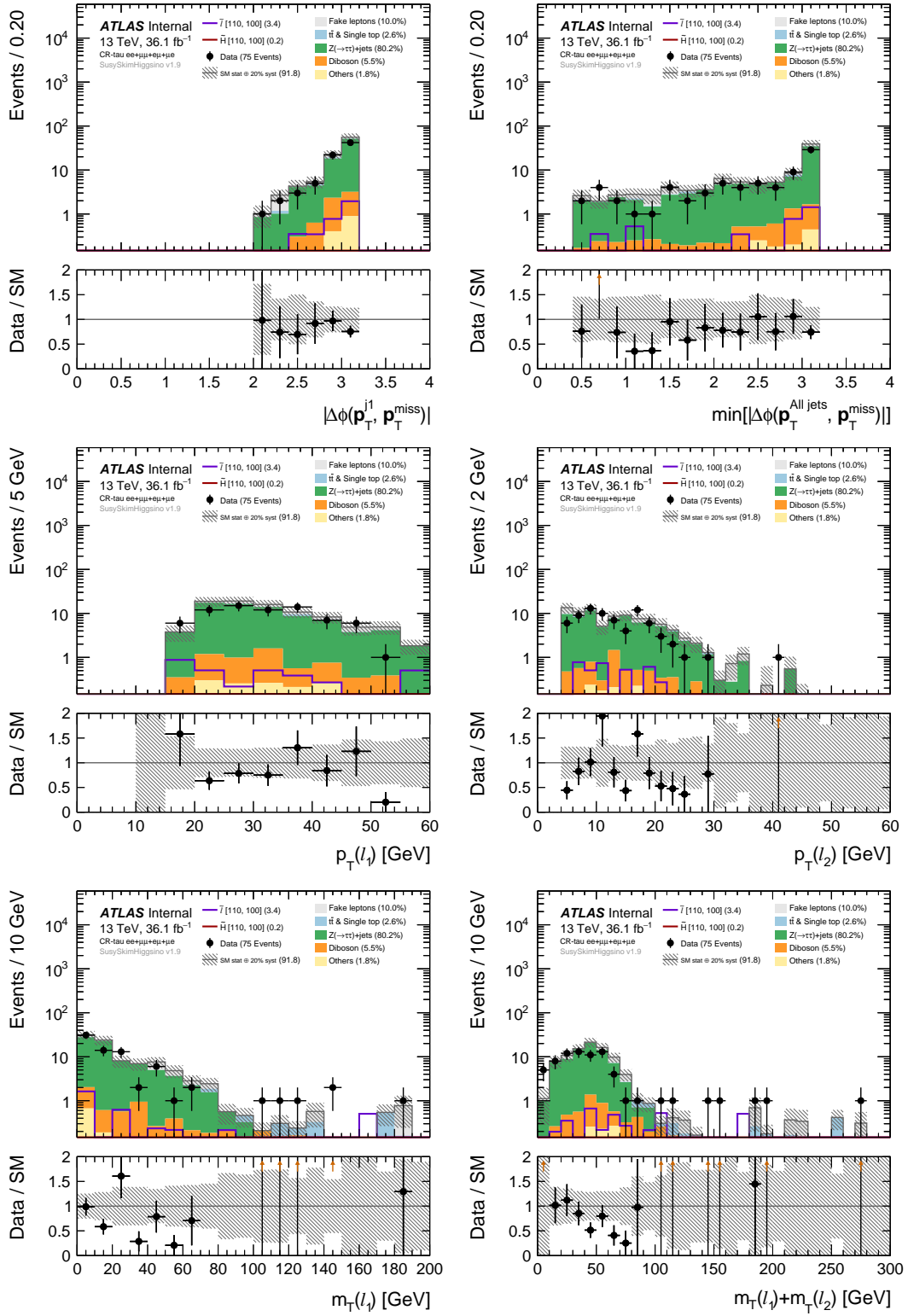


Figure 7.5:  $m_{T2}^{100}$ <sup>63</sup>

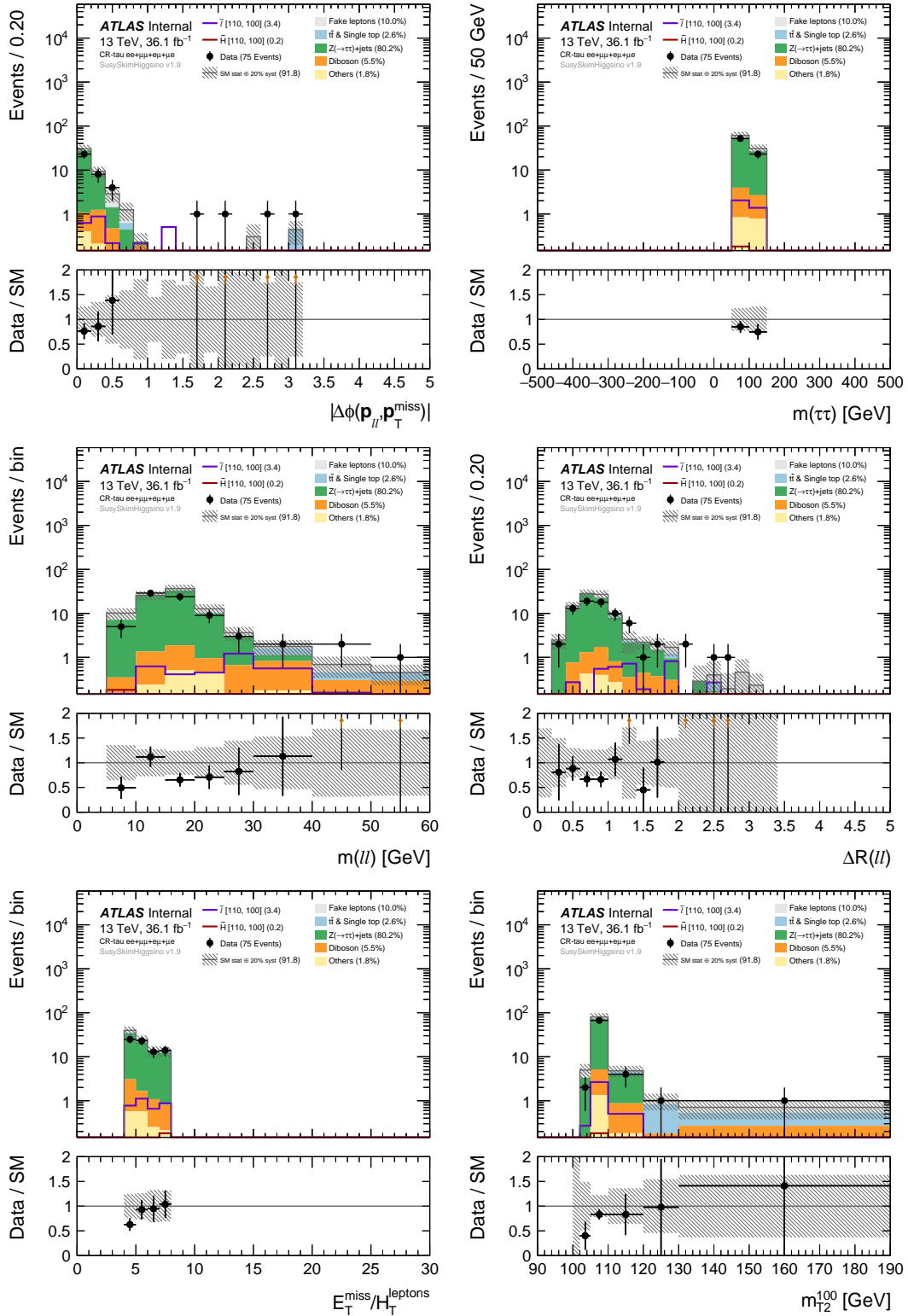
Figure 7.6: CR-top  $ee + \mu\mu + e\mu + \mu e$  channel, pre-fit distributions.



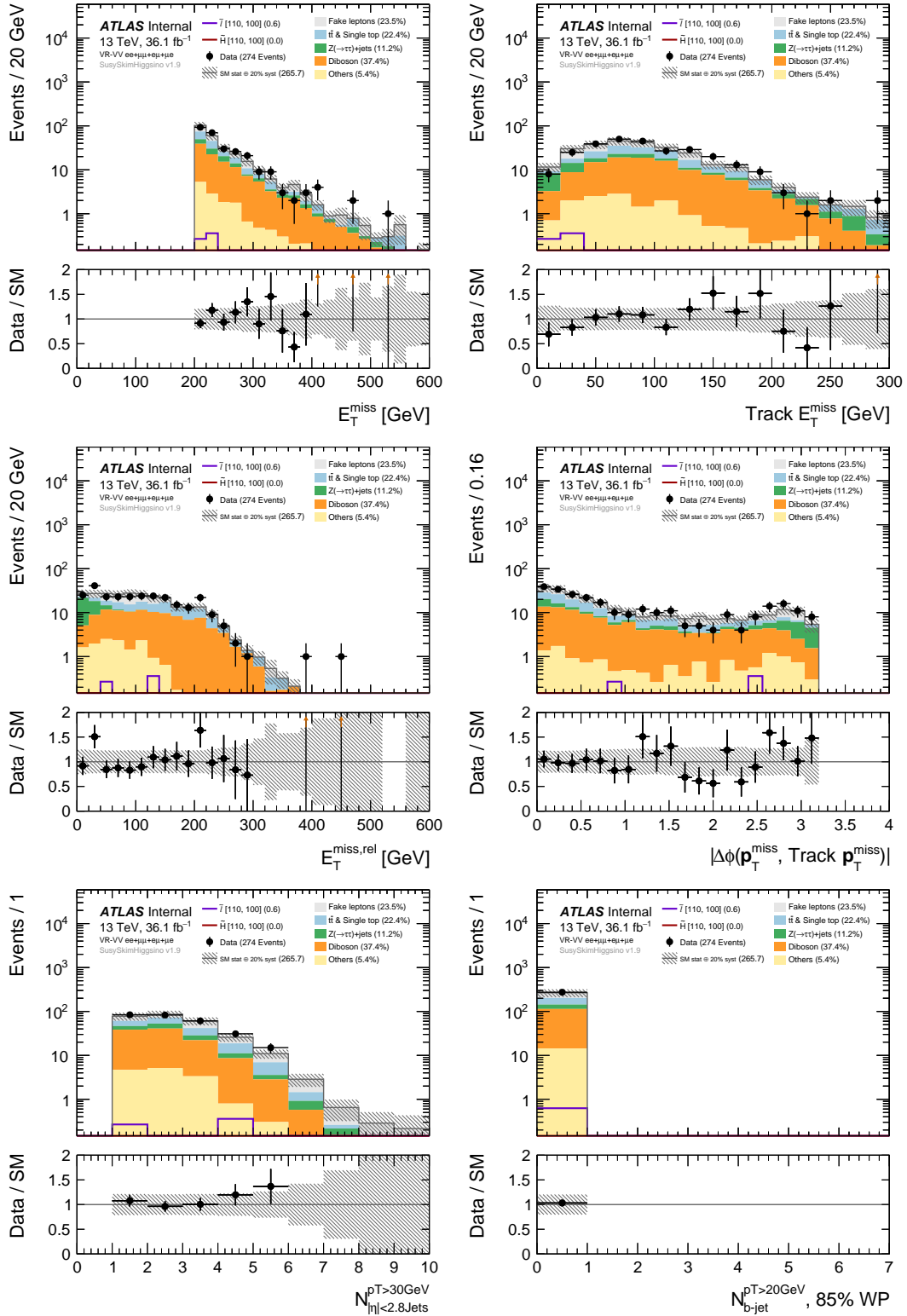
64  
Figure 7.7: CR-tau  $ee + \mu\mu + e\mu + \mu e$  channel, pre-fit distributions.



65  
Figure 7.8: CR-tau  $ee + \mu\mu + e\mu + \mu e$  channel, pre-fit distributions.



66  
Figure 7.9: CR-tau  $ee + \mu\mu + e\mu + \mu e$  channel, pre-fit distributions.



67  
Figure 7.10: VR-VV  $ee + \mu\mu + e\mu + \mu e$  channel, pre-fit distributions.

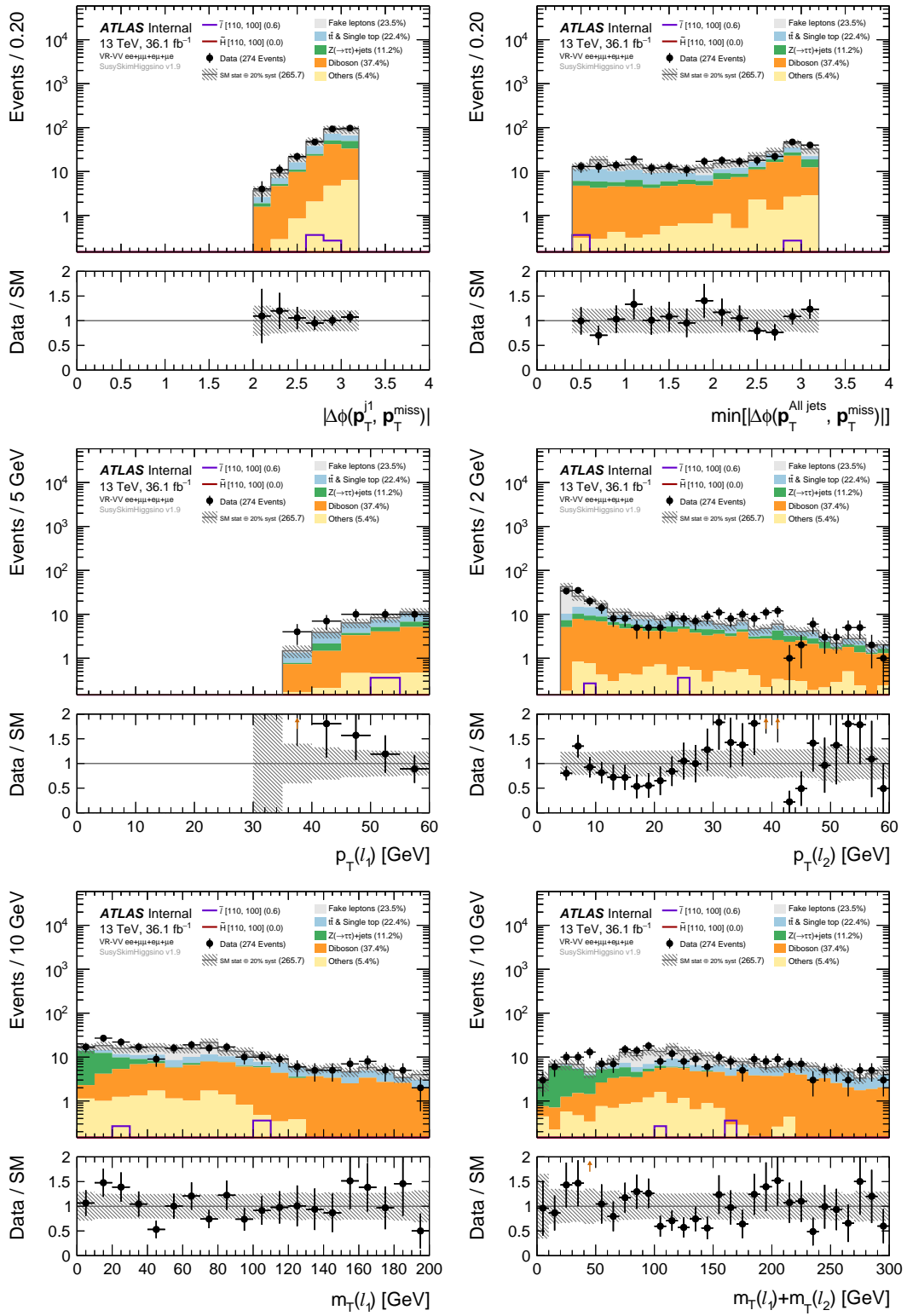
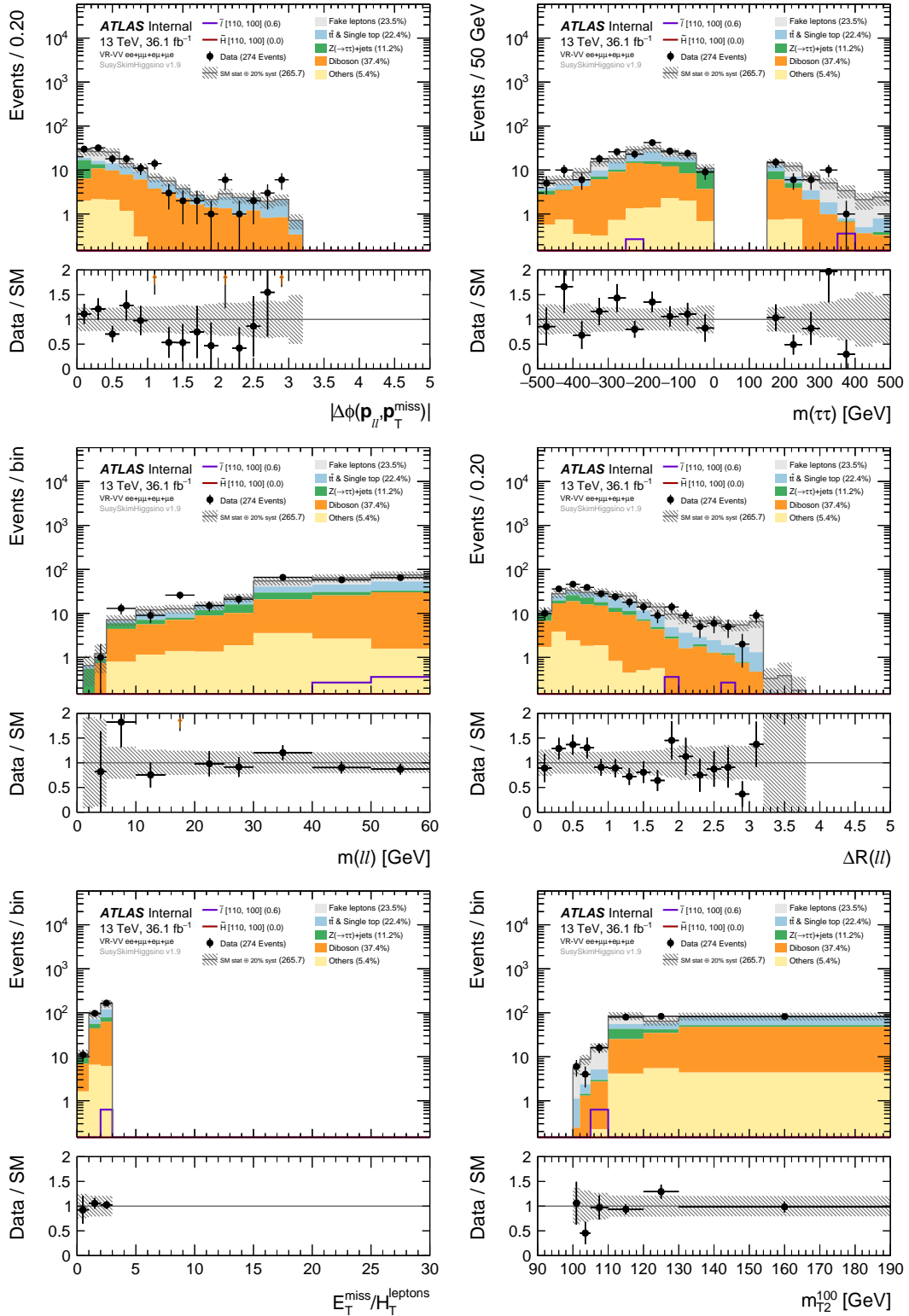


Figure 7.11: VR-VV  $ee + \mu\mu + e\mu + \mu e$  channel, pre-fit distributions.



69  
 Figure 7.12: VR-VV  $ee + \mu\mu + e\mu + \mu e$  channel, pre-fit distributions.

# **Chapter 8**

## **Systematic Uncertainties**

Talk about the sources of uncertainty and the estimates.

### **8.1 Experimental**

CP group uncertainties and fake factor uncertainties are the sources of experimental systematics

### **8.2 Theoretical**

In this section we will go over the theoretical systematics and both signal and background estimates.

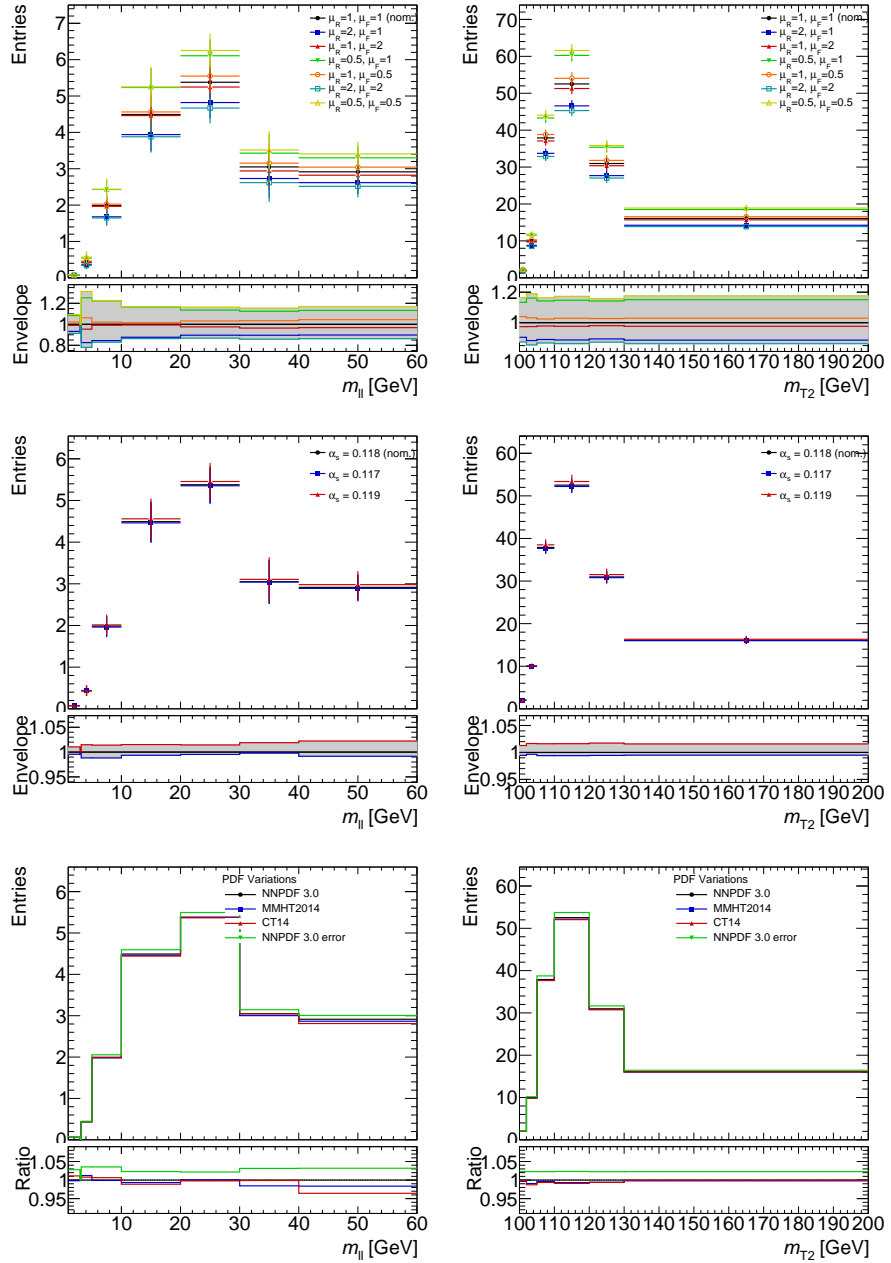


Figure 8.1: QCD scale,  $\alpha_s$  and PDF uncertainties on the shape and normalization of the diboson background in the Higgsino and slepton signal regions (with no lepton flavor requirement).

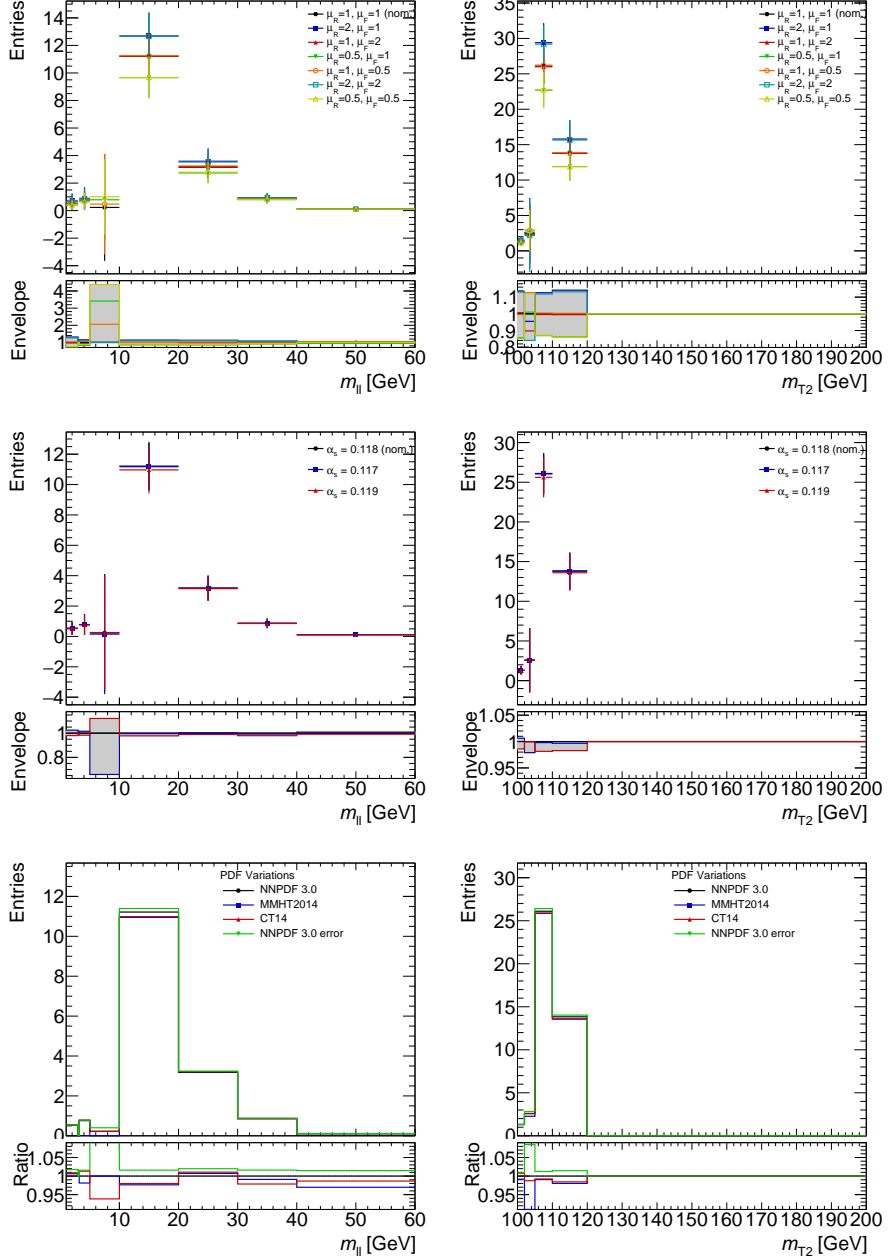


Figure 8.2: QCD scale,  $\alpha_s$  and PDF uncertainties on the shape and normalization of the  $Z \rightarrow \tau\tau$  background in the Higgsino and slepton signal regions (with no lepton flavor requirement).

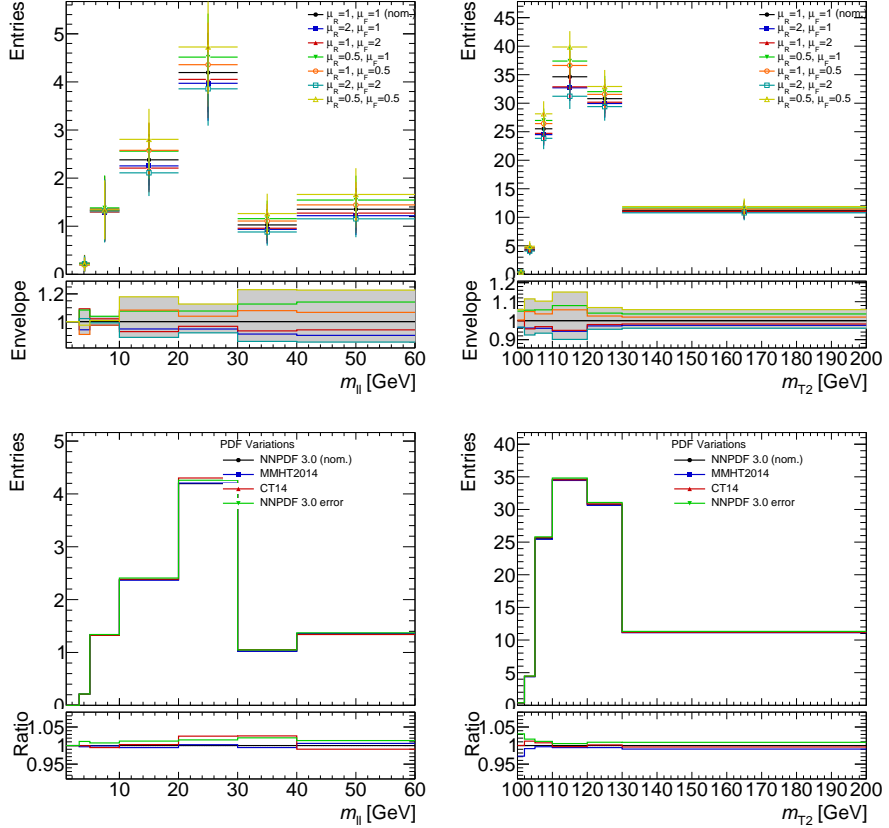


Figure 8.3: QCD scale and PDF uncertainties on the shape and normalization of the  $t\bar{t}$  background in the Higgsino and slepton signal regions (with no lepton flavour requirement).

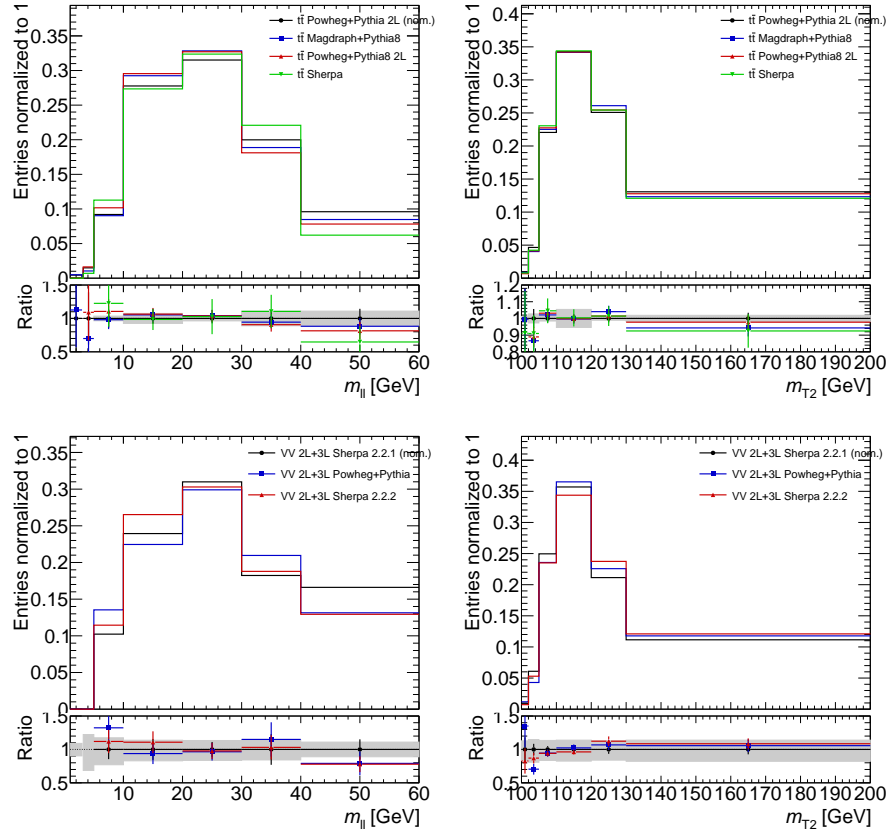


Figure 8.4: Comparison of the  $m_{\ell\ell}$  (left) and  $m_{T2}$  (right) shapes predicted by different  $t\bar{t}$  (top) and  $VV$  (bottom) MC generators, in the Higgsino and slepton signal regions. All distributions are normalized to the same number of entries. The gray band displayed in the ratio pad under each distribution represents the modeling uncertainty assigned to each background in each of the bins.

# **Chapter 9**

## **Statistical Analysis**

Explain all the things I don't yet understand about likelihood functions and such....

# **Chapter 10**

## **Results**

Model independent interpretations are shown as well as compressed higgsino and compressed slepton interpretations.

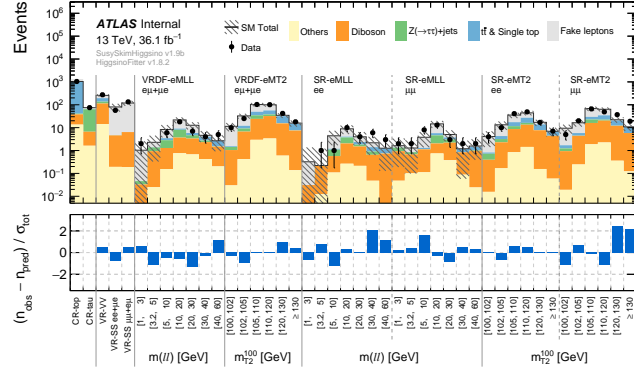


Figure 10.1: Summary of Monte Carlo yields in control, validation and signal regions in a background-only fit using data only in the two CRs to constrain the fit.

## 10.1 Compressed Higgsino

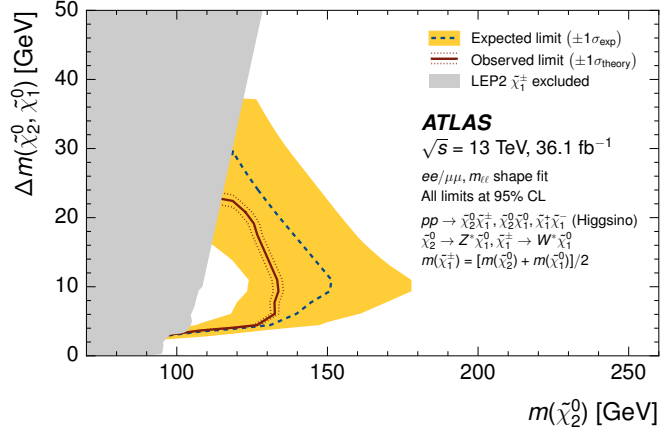


Figure 10.2: Expected 95% CL exclusion sensitivity (blue dashed line) with  $\pm 1\sigma_{\text{exp}}$  (yellow band) from experimental systematics and observed limits (red solid) with  $\pm 1\sigma_{\text{theory}}$  (dotted red) from signal cross section uncertainties. A shape fit of Higgsino signals to the  $m_{\ell\ell}$  spectrum is used to derive the limit is displayed in the  $m(\tilde{\chi}_2^0) - m(\tilde{\chi}_1^0)$  vs  $m(\tilde{\chi}_2^0)$  plane. The chargino  $\tilde{\chi}_1^\pm$  mass is assumed to be half way between the two lightest neutralinos. The grey region denotes the lower chargino mass limit from LEP [?].

## 10.2 Compressed Slepton

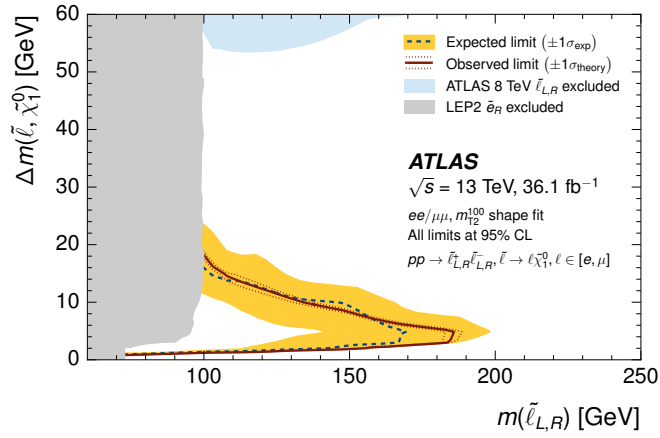


Figure 10.3: Expected 95% CL exclusion sensitivity (blue dashed line) with  $\pm 1\sigma_{\text{exp}}$  (yellow band) from experimental systematics and observed limits (red solid) with  $\pm 1\sigma_{\text{theory}}$  (dotted red) from signal cross section uncertainties. A shape fit of slepton signals to the  $m_{T2}^{100}$  spectrum is used to derive the limit projected into the  $m(\tilde{\ell}) - m(\tilde{\chi}_1^0)$  vs  $m(\tilde{\ell})$  plane. The slepton  $\tilde{\ell}$  refers to a 4-fold mass degenerate system of left- and right-handed selectron and smuon. The grey region denotes a conservative right-handed smuon  $\tilde{\mu}_R$  mass limit from LEP [?], while the blue region is the 4-fold mass degenerate slepton limit from ATLAS Run 1 [?].

# Chapter 11

## Conclusion

A search for supersymmetry in scenarios with compressed mass spectra was performed using ATLAS data collected in 2015 and 2016 at  $\sqrt(s)$  13 TeV, corresponding to  $36.1 fb^{-1}$ . We searched for directly produced electroweakinos and sleptons in events containing two soft, oppositely signed and same flavored leptons and including missing transverse momentum energy recoiling against initial state hadronic radiation. The directly produced electroweakinos and sleptons subsequently decay to their Standard Model partners and the lightest SUSY particle which is nearly degenerate in mass. No significant excess in data over Standard Model background was found; therefore, results were consistent with Standard Model prediction.

# **Appendix A**

## **Some Ancillary Stuff**

Ancillary material should be put in appendices, which appear after the bibliography.